

1      **Drivers of Observed Winter-Spring Sea-Ice and Snow Thickness at a**  
2      **Coastal Site in East Antarctica**

4      Diana Francis<sup>1\*</sup>, Ricardo Fonseca<sup>1</sup>, Narendra Nelli<sup>1</sup>, Petra Heil<sup>2,3,4</sup> Jonathan D. Wille<sup>5</sup>, Irina V.  
5      Gorodetskaya<sup>6</sup>, Robert A. Massom<sup>2,3,7</sup>

7      <sup>1</sup> Environmental and Geophysical Sciences (ENGEOS) Lab, Earth Sciences Department, Khalifa  
8      University, Abu Dhabi, 127788, United Arab Emirates

9      <sup>2</sup> Australian Antarctic Division, Department of Climate Change, Energy, the Environment and Water,  
10     Kingston, Tasmania, Australia

11     <sup>3</sup> Australian Antarctic Program Partnership, Institute for Marine and Antarctic Studies, University of  
12     Tasmania, Hobart, Tasmania, Australia

13     <sup>4</sup> Institute Snow and Avalanche Research, Swiss Federal Institute for Forest, Snow and Landscape  
14     Research, Davos, Switzerland

15     <sup>5</sup> Institute for Atmospheric and Climate Science, ETH Zurich, Zurich, Switzerland

16     <sup>6</sup> Interdisciplinary Centre of Marine and Environmental Research, University of Porto, Porto, Portugal

17     <sup>7</sup> The Australian Centre for Excellence in Antarctic Science, University of Tasmania, Hobart, Tasmania,  
18     Australia

19     \*Correspondence to: [diana.francis@ku.ac.ae](mailto:diana.francis@ku.ac.ae)

20      **Abstract:**

21      Antarctic sea ice and its snow cover play a pivotal role in regulating the global climate system  
22      through feedback on both the atmospheric and the oceanic circulations. Understanding the intricate  
23      interplay between atmospheric dynamics, mixed-layer properties, and sea ice is essential for  
24      accurate future climate change estimates. This study investigates the mechanisms behind the  
25      observed sea-ice and snow characteristics at a coastal site in East Antarctica using *in-situ*  
26      measurements in winter-spring 2022. The observed sea-ice thickness peaks at 1.16 m in mid-late  
27      October and drops to 0.06 m at the end of November, following the seasonal solar cycle. On the  
28      other hand, the snow thickness variability is impacted by atmospheric forcing, with significant  
29      contributions from precipitation, Foehn effects, blowing snow, and episodic warm and moist air  
30      intrusions, which can lead to changes of up to 0.08 m within a day for a field that is in the range  
31      0.02-0.18 m during July-November 2022. A high-resolution simulation with the Polar Weather  
32      Research and Forecasting model for the 14 July atmospheric river (AR), the only AR that occurred  
33      during the study period, reveals the presence of AR rapids and highlights the effects of katabatic  
34      winds from the Antarctic Plateau in slowing down the low-latitude air masses as they approach

35 the Antarctica coastline. The resulting convergence of the two air flows, with meridional wind  
36 speeds in excess of  $45 \text{ m s}^{-1}$ , leads to precipitation rates above  $3 \text{ mm hr}^{-1}$  around coastal Antarctica.  
37 The unsteady wind field in response to the passage of a deep low pressure system with a central  
38 pressure that dropped to 931 hPa triggers satellite-derived pack ice drift speeds in excess of  $60 \text{ km}$   
39  $\text{day}^{-1}$ , and promotes the opening up of a polynya in the Southern Ocean around  $64^\circ\text{S}, 45^\circ\text{E}$  from  
40 14 to 22 July. Our findings contribute to a better understanding of the complex interactions within  
41 the Antarctic climate system, providing valuable insights for climate modeling and future  
42 projections.

43

#### 44 **Keywords:**

45 Sea Ice, Snow Thickness, PolarWRF, Atmospheric River, Surface Mass Balance, Antarctica

46

## 47 **1. Introduction**

48 Sea ice, which forms from the freezing of seawater and covers 3-6% of the total surface area  
49 of the planet, plays multiple crucial roles in the Earth's climate system and high-latitude  
50 ecosystems (Thomas, 2017; Eayrs et al., 2019). Changes in the formation and melt rates, extent,  
51 seasonality and thickness of Antarctic sea ice - both in the form of drifting pack ice and less  
52 extensive stationary near-shore landfast ice (fast ice) attached to coastal margins, sea floor and  
53 grounded icebergs (Fraser et al., 2023) - substantially impact the heat and salinity content of the  
54 ocean, and hence the oceanic circulation (e.g., Haumann et al., 2016; Li and Fedorov, 2021). At  
55 the same time, breaks in the sea ice such as leads and recurrent and persistent polynyas (Barber  
56 and Massom, 2007; Francis et al. 2019, 2020; Fonseca et al., 2023) act as a thermal forcing (Guest,  
57 2021), directly impacting the atmospheric flow (Trusel et al., 2023; Zhang and Screen, 2021). Both  
58 oceanic and atmospheric forcing directly affect sea ice and its spatial extent, seasonality and  
59 thickness (Wang et al., 2020; Yang et al., 2021), within a finely-coupled interactive ocean-sea ice-  
60 atmosphere system. At the same time, decreases in sea-ice thickness (SIT), sea-ice extent (SIE),  
61 and its snow cover have strong potential to impact low-latitude weather patterns (England et al.,  
62 2020), disrupt the global surface energy balance (Riihelä et al., 2021), and amplify climate  
63 warming at high southern latitudes (Williams et al., 2023), leading to increased sea-ice loss that is  
64 likely to be further accelerated by poorly-understood ocean-ice-snow-atmosphere feedback  
65 mechanisms (Goosse et al., 2023).

66

67 The Antarctic sea ice-snow system is particularly impacted by two atmospheric processes: (1)  
68 strong katabatic winds that cascade seawards off the ice sheet and promote sublimation of the sea  
69 ice and its snow cover (Elvidge et al., 2020; Francis et al., 2023); and (2) a number of more  
70 ephemeral but influential extreme atmospheric events in the form of atmospheric rivers (ARs;  
71 Wille et al., 2025). Foehn effects are an important trigger of surface melting around Antarctica, as  
72 the adiabatic compression of the downslope flow can lead to a marked increase in surface

73 temperature in excess of 15 K (Bozkurt et al., 2018), while the associated strong winds can promote  
74 iceberg calving events (Miles et al., 2017). An AR is a narrow and highly elongated band of  
75 moisture-rich air that originates in the tropics and subtropics and propagates polewards into the  
76 mid- and high-latitudes (Wille et al., 2019; Gorodetskaya et al., 2020). ARs are associated with  
77 increased humidity and cloudiness, leading to an enhancement of the downward longwave  
78 radiation flux(Djouma and Holland, 2021), with the resulting increase in the surface net radiation  
79 flux giving a warming tendency and promoting surface melting (Gorodetskaya et al., 2013; Francis  
80 et al., 2020; Ghiz et al., 2021).

81  
82 There are several examples of ARs triggering ice and snow melt around Antarctica: e.g. in the  
83 Weddell Sea in 1973 and 2017 (Francis et al., 2020); off the Antarctic Peninsula in March 2015  
84 (Bozkurt et al., 2018) and February 2022 (Gorodetskaya et al., 2023); around the Amery Ice Shelf  
85 in September 2019 (Francis et al., 2021), in West Antarctica (Francis et al., 2023); and in the Ross  
86 Sea (Fonseca et al., 2023). The recent study of Liang et al. (2023) highlights that the largest impact  
87 of ARs on sea ice is found on the marginal ice zone, where the SIE reduction may exceed 10%  
88 day<sup>-1</sup>. Reduced coastal offshore SIE may also foster a deeper penetration of the low-latitude air  
89 onto the inland ice sheet as it enhances moisture availability, as is the case in the March 2022 “heat  
90 wave” in East Antarctica (Wille et al., 2024a,b). While ARs themselves are relatively rare and  
91 short-lived in coastal Antarctica, with a frequency of ~3 days year<sup>-1</sup> at any given location, the warm  
92 and moist air masses they transport can make a substantial contribution to the surface mass balance  
93 (SMB) and are linked to extreme precipitation events (Massom et al., 2004; Wille et al. 2021,  
94 2025). For example, in East Antarctica, a series of ARs delivered an estimated 44% of the total  
95 mean-annual snow accumulation to the high interior ice sheet over an 18-day period in the austral  
96 summer of 2001/2 (Massom et al., 2004), and AR-associated rainfall has exceeded 30% of the  
97 total annual precipitation (McLennan et al. 2022, 2023). These studies highlight the impacts of  
98 extreme weather events on the coupled Antarctic ocean-ice-snow-atmosphere system and stress  
99 the need to better understand the role of low-latitude air incursions on the SMB and on the state of  
100 both the Antarctic Ice Sheet and its surrounding sea-ice cover - and how these may change in a  
101 warming climate.

102  
103 The effects of the atmospheric forcing, such as that associated with extreme weather episodes,  
104 on the sea-ice-snow-air coupling system can be inferred through the analysis of *in-situ*  
105 measurements of SIT and snow thickness (ST). This is achieved in this study through the  
106 deployment of an autonomous Snow Ice Mass Balance Array (SIMBA) buoy (Jackson et al., 2013)  
107 from July to November 2022 at a coastal fast ice site close to Mawson Station in East Antarctica  
108 (67.5912°S, 62.8563°E), which will be denoted as “Khalifa SIMBA site on fast ice off Mawson  
109 Station” throughout the manuscript. This station is selected as it has amongst the highest AR  
110 frequency in the continent, also with a statistically significant positive trend in AR frequency and  
111 intensity during 1980-2020 (Wille et al., 2025). The overall aim of this work is to further our  
112 understanding of the temporal evolution of the thickness and vertical structure of coastal sea ice

113 and its snow cover in East Antarctica, and over a six-month period spanning austral winter through  
114 late spring when ARs are more frequent in the region (Wille et al., 2025). This study is timely  
115 given the precipitous downward trend in Antarctic SIE since 2016 (Parkinson, 2019), an  
116 extraordinary record-low annual minimum in February 2023 and a sudden departure to major sea-  
117 ice deficits through the winters of 2023 and 2024 (Reid et al., 2024). This turn of events suggests  
118 that Antarctic sea ice has abruptly shifted into a new low-extent regime (Purich and Doddridge,  
119 2023; Hobbs et al., 2024). Much less well known - though no less important - are the thicknesses  
120 of the ice and its ST and whether these are changing. Obtaining more accurate and complete  
121 information on the Antarctic SIT distribution and its ST and precipitation rates - and the factors  
122 and processes controlling them - is a critical high priority in climate science, particularly in light  
123 of climate variability and change (Webster et al., 2018; Meredith et al., 2021).

124  
125 Accurate knowledge of SIT, SIE and concentration is needed to estimate sea-ice volume, a field  
126 that is directly parameterized in numerical models (Massonnet et al., 2013; Zhang, 2014; Schroeter  
127 and Sandery, 2022) and that exhibits large uncertainties (Maksym et al. 2008, 2012). Satellite radar  
128 and laser altimeters hold the key to large-scale estimation and monitoring of both SIT (e.g.,  
129 Fonseca et al., 2023) and ST (Kacimi and Kwok, 2020). Kurtz and Markus (2012) used the  
130 measurements collected by the Ice, Cloud, and land Elevation Satellite (ICESat) to estimate the  
131 ice thickness around Antarctica. A comparison with ship-based observations revealed a mean  
132 difference of 0.15 m for the period 2003-2008, with a typical SIT of 1-1.5 m. Kacimi and Kwok  
133 (2020), using both laser (ICESat-2) and radar (CryoSat-2) altimeter estimates for the period 1 April  
134 to 16 November 2019, found the thickest sea ice in the western Weddell Sea sector (predominantly  
135 multi-year sea ice), with a mean thickness of 2 m, and the thinnest ice around polynyas in the Ross  
136 Sea and off the Ronne Ice Shelf. Coincident use of laser and radar altimetry also enables basin-  
137 scale estimates of ST. The thickest snow was again observed in the western Weddell Sea  
138 ( $0.228 \pm 12.4$  m in May) and the coastal region of the Amundsen-Bellingshausen seas sector  
139 ( $0.314 \pm 23.1$  m in September), while the thinnest was in the Ross Sea ( $0.0735 \pm 4.30$  m in April)  
140 and the eastern Weddell Sea ( $0.0821 \pm 5.81$  m in June) (Kacimi and Kwok, 2020). These studies  
141 focused on pack ice, but a similar range of values has been estimated for the thickness of fast ice,  
142 such as off Mawson (Li et al., 2022) and Davis (Heil, 2006) stations in East Antarctica. The  
143 SIMBA buoy observations provide invaluable gap-filling information on the temporal evolution  
144 and state of the snow-sea ice system and its response to atmospheric and oceanic variability. They  
145 are also crucial to both (1) calibrate the key satellite SIT and ST data products, and (2) evaluate  
146 and improve numerical idealized column and weather forecasting models (Hu et al., 2023; Plante  
147 et al., 2024; Sledd et al., 2024; Wang et al., 2024a). Such steps are needed to rectify present low  
148 confidence in model projections of future climate and Antarctic sea-ice conditions that currently  
149 diverge for different models and scenarios (Roach et al., 2020).

150  
151 While there are a number of studies on *in-situ* SIT and ST measurements around Antarctica  
152 (e.g., Worby et al., 2011; Xie et al., 2011; Liao et al., 2022), the area of East Antarctica around

153 Mawson Station, where extreme precipitation events in the form of ARs have become more  
154 frequent and intense in the recent decades (Wille et al., 2025), has not been sampled. In addition,  
155 these works do not delve deep into the processes responsible for the observed changes in SIT and  
156 ST, which is a necessary step for refining Antarctic climate projections. The objectives of this  
157 study are twofold: (1) to identify the mechanisms behind the variability of the *in-situ* measured  
158 SIT and ST at Mawson Station during July-November 2022, and compare the measured values  
159 with those estimated from remote sensing assets; and (ii) to perform high-resolution numerical  
160 simulations for selected periods during the measurement campaign, in particular during extreme  
161 weather events, to gain further insight into the role of atmospheric forcing on the SIT and ST. This  
162 study will therefore contribute to further our understanding on the variability of the SIT and ST in  
163 coastal Antarctica and the respective driver processes.

164

165 This paper is structured as follows. The observational datasets and model outputs and products  
166 considered, and analysis techniques used, are described in Section 2. The measurements of SIT  
167 and ST, including their variability and the mechanisms behind them, are discussed in Section 3.  
168 Section 4 provides a case-study analysis of the period 11-16 July 2022, while in Section 5 the main  
169 findings of the work are outlined and discussed.

## 170 **2. Methodology & Diagnostics**

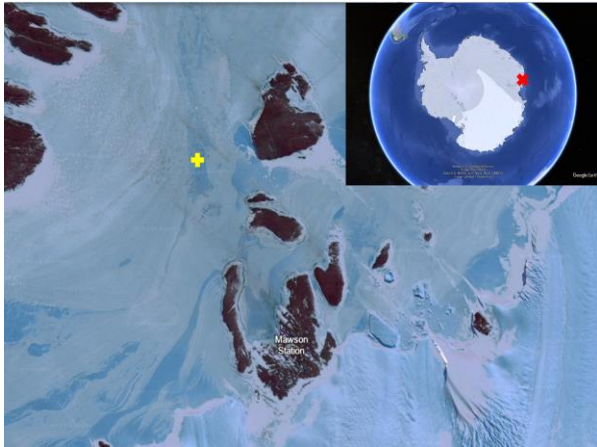
### 171 **2.1. *In-Situ* Measurements at Khalifa SIMBA site off Mawson Station**

172 *In-situ* measurements of SIT and ST are obtained using a sea-ice mass-balance (SIMBA) unit  
173 (Jackson et al., 2013). This SIMBA is deployed on landfast ice offshore from Mawson Station at  
174 67.5912°S, 62.8563°E (Fig. 1a) on 7 July 2022, and remained *in-situ* until 7 December 2022. The  
175 SIMBA unit, Fig. 1b, consists of a 5 m-long thermistor string with a 0.02 m sensor spacing, a  
176 barometer for surface air pressure, and an external sensor for near-surface ambient air temperature  
177 (Jackson et al., 2013). During deployment, manual measurements of SIT and ST, as well as  
178 freeboard, are recorded. The positions of the sensors relative to the interfaces are noted to establish  
179 the initial state (on 7 July 2022). The measured SIT upon deployment is 0.988 m, the ST on top of  
180 the sea ice is 0.156 m, and the sea-ice freeboard is 0.046 m. No manual validation or calibration is  
181 conducted during the measurement period of 7 July - 7 December 2022.

182

(a)

(b)



(a)



(b)

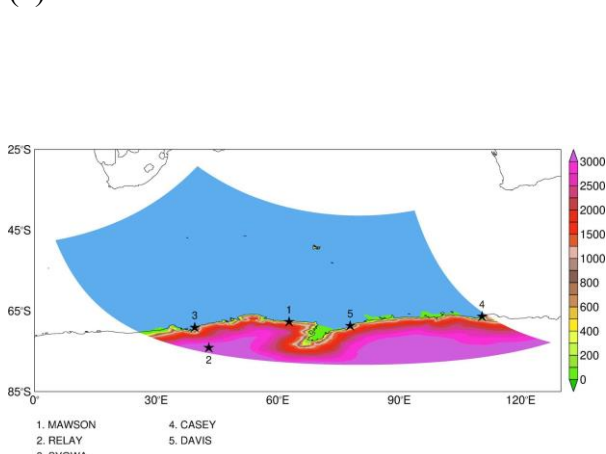
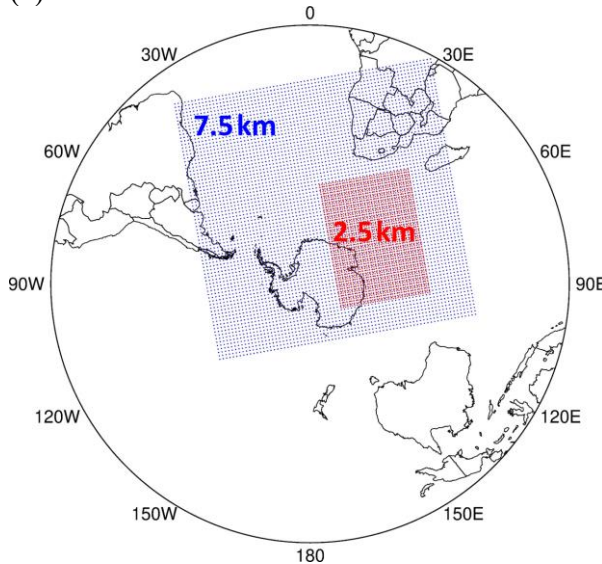


**Figure 1: SIMBA Deployment Site and PolarWRF Simulation:** (a) SIMBA deployment site (yellow cross) on the fast ice about 1.8 km off Mawson Station. Image source: Landsat 8 acquired on 19 November 2022. The red cross in the inset image, taken from Google Earth Pro, shows where Mawson Station is located in Antarctica. (b) SIMBA instrument prior to deployment. Image credit: Peter Caithness. (c) Spatial extent of the 7.5 km (blue) and 2.5 km (red) PWRF grids used in the numerical simulations. (d) Spatial extent and orography (m) of the 2.5 km PWRF grid. The stars highlight the location of the five weather stations considered in this work

183

184 The accuracy of the bus-addressable digital temperature sensing integrated circuit is  $\pm 0.0625$  K. A  
 185 resistor is mounted directly underneath each thermistor sensor. A low voltage power supply (8 V)  
 186 is connected to each sensor, to gently heat the sensor and its immediate surroundings. In this study,

187 heating is applied to the sensor chain for durations of 30 s and 120 s once per day, with four vertical  
188 temperature profiles without heating also recorded daily. In this study, SIMBA data from 8 July to  
189 30 November 2022 are used to assess the evolution of SIT and ST at the site. The measurements  
190 are shown in Fig. 2. For the sensors 6 through 126, the actual temperature and the temperature rise  
191 after 120 s heating are given in Fig. 2a and 2b, respectively, with Fig. 2c showing the difference  
192 between the measurements of two adjacent temperature sensors after applying the heating.  
193

194 The vertical temperature gradients in the air above the surface and in the water below the ice  
195 bottom are generally very small (Jackson et al., 2013; Hoppmann et al., 2015; Liao et al., 2018).  
196 After 120 s of heating, the rise in temperature is approximately 10 times higher in air than in ice  
197 and water (Jackson et al., 2013). For any two adjacent sensors in the ice, and following the  
198 algorithm detailed in Liao et al. (2018) based on a physical model applied to the SIMBA  
199 measurements, the temperature difference should be  $\leq 0.1875$  K, whereas for two adjacent sensors  
200 in snow, the temperature difference should be  $\geq 0.4375$  K. These thresholds are applied to the  
201 temperature differences between adjacent sensors in the heating profile to identify the air-snow  
202 and snow-ice interfaces (Jackson et al., 2013; Hoppmann et al., 2015; Liao et al., 2018). The ice-  
203 water interface is identified using a statistical approach based on Liao et al. (2018). A section of  
204 the thermistor string, spanning from the top of the sea ice to a few sensors below the water, is  
205 selected. The seawater temperature near the ice bottom remains stable around the freezing point  
206 ( $T_f$ ). The temperature readings from this section are analyzed as a time series, and the most frequent  
207 value is identified as  $T_f$ . Scanning from bottom up, the last sensor close to  $T_f$  is identified as the  
208 ice bottom. The allowed temperature difference is 1.5 times the thermistor resolution of 0.0625 K.  
209 The temporal evolutions of the three interface locations are plotted in Figs. 2a-c.

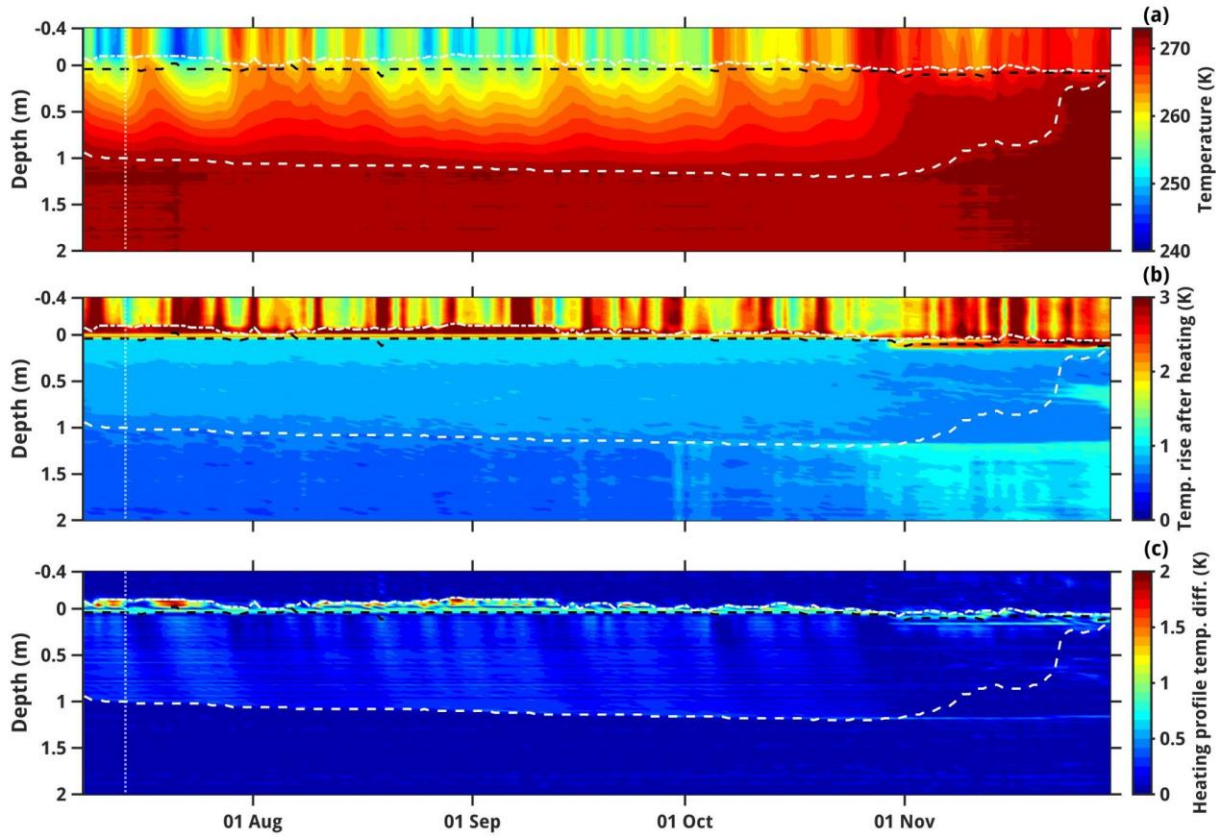


**Figure 2: SIMBA measurements:** (a) Temperature (K) evolution from the top of the chain through the ice down into the water (the zero line on the y-axis is at the snow-ice interface). (b) Temperature rise (K) after heating for 120 s. (c) Temperature difference (K) between adjacent sensors after applying the heating for 120 s. The vertical white dotted line indicates the day of AR occurrence at the site, 14 July. The horizontal dotted white line, black dashed line, and white dashed line give the air-snow (AS), snow-ice (SI), and ice-water (IW) interfaces, respectively.

210

## 211 2.2. Observational and Reanalysis Datasets

212 In addition to *in-situ* SIT and ST measurements, three observational datasets are considered in  
 213 this work: (i) satellite-derived SIE and sea-ice velocity; (ii) ground-based observations at five  
 214 weather stations, namely Mawson, Syowa, Relay, Casey, and Davis (Fig. 1d); and (iii) twice daily  
 215 sounding profiles at the Mawson, Syowa, Casey, and Davis stations (stations #1 and 3-5 in Fig.  
 216 1d). Data from the fifth generation of the European Centre for Medium Range Weather Forecasting  
 217 reanalysis (ERA-5; Hersbach et al., 2020) are used to investigate the large-scale circulation and  
 218 SMB during the study period. ERA-5 is regarded as one of the best reanalysis products currently

219 available over Antarctica and the Southern Ocean (Gossart et al., 2019; Dong et al., 2020). All of  
220 these products are listed in Table 1.

221

Dataset	Specifications
<b>In-situ Sea-Ice Thickness and Snow Thickness</b>	SIT and ST measurements just offshore of Mawson Station (67.5912°S, 62.8563°E) using a SIMBA unit; data available from 7 July to 7 December 2022
<b>Sea-Ice Extent</b>	Satellite-derived daily SIE at 3.125 km resolution; data available from June 2002 - Present
<b>Sea-Ice Velocity</b>	Satellite-derived daily sea-ice velocity at 62.5 km resolution; data available from December 2009 - Present
<b>Weather Station Data</b>	Ground-based observations at Mawson (67.6017°S, 62.8753°E; January 1954 - Present), Relay (74.017°S, 43.062°E; November 2021 - Present), Syowa (69.0053°S, 39.5811°E; January 1994 - Present), Casey (66.2825°S, 110.5231°E; February 1989 - Present), and Davis (68.5744°S, 77.9672°E; January 1957 - Present) Stations
<b>Sounding Profiles</b>	Twice daily at Mawson (67.6017°S, 62.8753°E; January 1954 - Present), Syowa (69.0053°S, 39.5811°E; January 2021 - Present), Casey (66.2825°S, 110.5231°E; February 1989 - Present), and Davis (68.5744°S, 77.9672°E; January 1957 - Present) Stations
<b>ERA-5 reanalysis</b>	Hourly products at $0.25^\circ \times 0.25^\circ$ ( $\sim 27$ km) spatial resolution; available from January 1940 - Present

222  
223 **Table 1: Observational and Reanalysis Datasets:** List of observational and reanalysis datasets used in  
224 this study.

225  
226 Daily SIE is derived from the measurements of sea-ice concentration collected by the  
227 Advanced Microwave Scanning Radiometer for Earth Observing Systems (AMSR-E) onboard the  
228 National Aeronautics and Space Administration (NASA) Aqua satellite from June 2002 to October  
229 2011, and from the observations taken by the AMSR2 onboard Japan Aerospace and Exploration  
230 Agency's Global Change Observation Mission - Water (GCOM-W) satellite from July 2012 to  
231 present (Spreen et al., 2008). Sea-ice velocity vectors, on the other hand, are obtained from the  
232 measurements collected by the Special Sensor Microwave Imager/Sounder onboard the United  
233 States Air Force Defense Meteorological Satellite Program, the Advanced Scatterometer onboard  
234 the European Space Agency's Meteorological Operational satellite, and the GCOM-W AMSR2  
235 (Lavergne et al., 2010). Both the SIE and sea-ice velocity products are used to gain insight into  
236 the effects of the warm and moist air intrusions on the sea-ice state around Mawson Station, as

237 performed in previous studies for other parts of Antarctica (e.g., Francis et al., 2021; Fonseca et  
238 al., 2023).  
239

240 *In-situ* observations at multiple Automatic Weather Stations (AWSs) are used in the analysis  
241 and model evaluation (Fig. 1d). These include: (i) 1-minute 2-m air temperature and humidity, 10-  
242 m horizontal wind velocity, and sea-level pressure (SLP) observations at the Australian Antarctic  
243 stations of Mawson, Casey, and Davis; (ii) 1-minute measurements of meteorological parameters  
244 (2-m air temperature, SLP, 10-m horizontal wind velocity, and 2-m relative humidity) and  
245 radiation fluxes (surface upward and downward and shortwave and longwave) at the coastal Syowa  
246 Station; and (iii) 10-minute SLP, horizontal wind velocity, and 2-m air temperature and relative  
247 humidity observations at the inland Relay Station. Also analyzed are data from atmospheric  
248 sounding profiles acquired twice daily (at 00 and 12 UTC) at the Mawson, Syowa, Casey, and  
249 Davis stations.

## 250 2.3. Numerical Models

251 Here we use version 4.3.3 of the Polar PWRF (Weather Research and Forecasting) model, a  
252 version of the WRF model (Skamarock et al., 2019) optimized for the polar regions (Bromwich et  
253 al., 2013; Hines et al., 2021; Xue et al., 2022; Zou et al., 2023), to simulate and investigate the AR  
254 that impacted the Mac Robertson Land region on 14 July 2022. The model is run in a nested  
255 configuration, with a 7.5km horizontal resolution grid domain comprising Antarctica, the Southern  
256 Atlantic Ocean, southern Africa and the southwestern Indian Ocean, and a 2.5 km horizontal  
257 resolution grid domain extending from the Southern Ocean just south of South Africa around 30°E  
258 into coastal East Antarctica as far east as approximately 120°E (Fig. 1c). The choice of resolution,  
259 in particular the 2.5 km grid that covers the bulk of the AR and associated warm and moist air  
260 intrusion into East Antarctica, reflects the findings of Box et al. (2023) and Francis et al. (2024).  
261 These studies stressed the need to properly resolve the fine-scale structure of an AR due to the  
262 possible presence of AR rapid-like features embedded in the convective region, which can generate  
263 copious amounts of precipitation and hence have a substantial impact on the SMB of the ice. AR  
264 rapids are narrow (5-15 km wide), elongated (100-200 km long) and shallow (~3 km deep) linear  
265 features within the AR that propagate at high speed ( $>30 \text{ m s}^{-1}$ ) and last for more than 24 h. They  
266 have been reported for an AR that impacted Greenland in September 2017 (Box et al., 2023) and  
267 another that wreaked havoc in the Middle East in April 2023 (Francis et al., 2024). AR rapids are  
268 distinct from mesoscale convective systems (MCSs; Houze, 2004; Feng et al., 2021; Nelli et al.,  
269 2021), which propagate at a slower speed ( $10-20 \text{ m s}^{-1}$ ), typically do not last as long (6-10 h), and  
270 generate broader (as opposed to linear) precipitation structures.

271 PWRF is run from 10 July 2022 at 00 UTC to 17 July 2022 at 00 UTC, comprising the only AR  
272 that impacted the site during July-November 2022, with the first day regarded as spin-up and the  
273 output discarded. The hourly outputs of the 7.5 km and 2.5 km grids are used for analysis. The  
274 physics schemes selected, listed in Table 2, reflect the optimal model configuration for Antarctica  
275

276 and the Southern Ocean (Zou et al. 2021a, 2021b, 2023). In order to prevent the large-scales in the  
 277 model from drifting from the forcing fields, spectral nudging (Attada et al., 2021) is employed in  
 278 both grids for spatial scales  $\gtrsim 1,000$  km above  $\sim 800$  hPa and excluding the boundary layer. Fields  
 279 nudged include the horizontal wind components, the potential temperature perturbation, and the  
 280 geopotential height. In the vertical, 60 levels are considered, with the lowest level above the surface  
 281 at  $\sim 27$  m and roughly 20 levels in the range of  $\sim 1$ -6 km. The higher resolution in the low- to mid-  
 282 troposphere is crucial to correctly representing the fine-scale variability of the warm and moist air  
 283 masses impacting the site, and associated cloud processes (Rauber et al., 2020; Finlon et al., 2020).  
 284

Physics Scheme	Option Selected
<b>Cloud Microphysics</b>	Two-moment Morrison-Milbrandt P3 (Morrison and Milbrandt, 2015), with Vignon adjustment to improve the simulation of mid-level mixed-phase clouds over the Southern Ocean (Hines et al., 2021; Vignon et al., 2021)
<b>Planetary Boundary Layer</b>	Mellor-Yamada-Nakanishi-Niino level 1.5 (MYNN; Nakanishi and Niino, 2006)
<b>Radiation</b>	Rapid Radiative Transfer Model for Global Circulation Models (Iacono et al., 2008) for shortwave and longwave radiation
<b>Cumulus</b>	Kain-Fritsch (Kain, 2004) with subgrid-scale cloud feedbacks to radiation (Alapaty et al., 2012) only in 7.5 km grid
<b>Land Surface Model (LSM)</b>	Noah LSM (Chen and Dudhia, 2001; Tewari et al., 2004)
<b>Sea Surface Temperature (SST)</b>	6-hourly ERA-5 SSTs + Zeng and Beljaars (2005) surface skin temperature scheme

285  
 286 **Table 2: WRF Experimental Setup:** Physics scheme used in the WRF simulation.  
 287  
 288 PWRF is driven by 6-h ERA-5 data, with the SSTs and SIE used in the simulations taken from  
 289 ERA-5. Due to the lack of availability of SIT in ERA-5, the model's default SIT value of 3 m is  
 290 used in all sea-ice covered grid-boxes. The sea-ice albedo is parameterized as a function of air and  
 291 skin temperature following Mills (2011), with the model explicitly predicting ST on sea ice. A  
 292 sensitivity experiment is performed in which a more realistic representation of SIE and SIT is  
 293 considered. In particular, satellite-derived values are used for SIE, extracted from the 3.125 km-  
 294 resolution daily product available at the University of Bremen website (UoB, 2024), while the SIT  
 295 estimates at Mawson are employed at all sea-ice covered pixels. A similar model performance is  
 296 obtained with respect to the *in-situ* observations (not shown). Therefore, and for consistency with

297 the atmospheric forcing, the ERA-5's SIE and the PWRF's default SIT values are used in the  
298 model runs.

299

300 The moisture sources that contributed to the AR during 11-16 July 2022 are diagnosed based  
301 on 96-h back-trajectories obtained with the Hybrid Single-Particle Lagrangian Integrated  
302 Trajectory (HYSPLIT; Stein et al., 2015) model driven by ERA-5 reanalysis data.

303 **2.4. Diagnostics and Metrics**

304 The performance of the PWRF model is assessed with the verification diagnostics proposed  
305 by Koh et al. (2012) outlined in Supplement Section S1. In addition to the model bias, the two key  
306 skill scores are (1) the normalized bias  $\mu$ , defined as the ratio of the bias to the standard deviation  
307 of the discrepancy between the model forecasts and observations; and (2) the normalized error  
308 variance  $\alpha$ , which accounts for both phase and amplitude errors. When  $|\mu| < 0.5$  the model biases  
309 can be regarded as not significant, while when  $\alpha < 1$ , the model forecasts are deemed to be  
310 practically useful.

311 ARs are identified based on the Integrated Vapour Transport (IVT;  $\text{kg m}^{-1} \text{s}^{-1}$ ), which is the  
312 column integral of the water-vapour flux advected by the horizontal wind. It is quantified as

313 
$$IVT = \sqrt{\left(\frac{1}{g} \int_{1000 \text{ hPa}}^{200 \text{ hPa}} q u \, dp\right)^2 + \left(\frac{1}{g} \int_{1000 \text{ hPa}}^{200 \text{ hPa}} q v \, dp\right)^2} \quad (1)$$

314 In equation (1),  $g$  is the gravitational acceleration ( $9.80665 \text{ m s}^{-2}$ ),  $q$  is the specific humidity ( $\text{kg kg}^{-1}$ ),  $u$  is the zonal wind speed ( $\text{m s}^{-1}$ ),  $v$  is the meridional wind speed ( $\text{m s}^{-1}$ ), and  $dp$  is the  
315 pressure difference between adjacent vertical levels (hPa). The criteria of Wille et al. (2021)  
316 applied to ERA-5 data are used here to identify ARs. In particular, IVT has to exceed the 98<sup>th</sup>  
317 percentile extracted for 1979-2022 at a given grid-box, and a minimum latitudinal extent of 20° is  
318 required for the feature to be considered an AR. During the July to November 2022 study period,  
319 the Khalifa SIMBA site on fast ice off Mawson Station is affected by one AR, on 14 July. This  
320 event is selected for more in-depth analysis and modeling in Section 4. Large-scale circulation  
321 patterns that favour ARs, including the presence of blocking and interaction with tropopause polar  
322 vortices (TPVs), are also explored. Further details regarding the metrics used to diagnose them are  
323 given in Supplementary Sections S2-S3.

325

326 The extratropical circulation can be modulated by tropical forcing, such as thermal (heating  
327 and cooling) anomalies (Hoskins and Karoly, 1981; Hoskins et al., 2012). In order to explore  
328 whether this occurs during the case study, the stationary wave activity flux that indicates the  
329 direction of the anomalous stationary Rossby wave propagation, defined in Takaya and Nakamura  
330 (2001), is derived equations (2a-b) and plotted.

331 
$$W_X = \frac{p \cos(\phi)}{2|u|} \left\{ \frac{u}{a^2 \cos(\phi)^2} \left[ \left( \frac{\partial \psi'}{\partial \lambda} \right)^2 - \psi' \frac{\partial^2 \psi'}{\partial \lambda^2} \right] + \frac{v}{a^2 \cos(\phi)} \left[ \frac{\partial \psi'}{\partial \lambda} \frac{\partial \psi'}{\partial \phi} - \psi' \frac{\partial^2 \psi'}{\partial \lambda \partial \phi} \right] \right\} \quad (2a)$$

332

333 
$$W_Y = \frac{p \cos(\phi)}{2|u|} \left\{ \frac{u}{a^2 \cos(\phi)} \left[ \frac{\partial \psi'}{\partial \lambda} \frac{\partial \psi'}{\partial \phi} - \psi' \frac{\partial^2 \psi'}{\partial \lambda \partial \phi} \right] + \frac{v}{a^2} \left[ \left( \frac{\partial \psi'}{\partial \phi} \right)^2 - \psi' \frac{\partial^2 \psi'}{\partial \phi^2} \right] \right\} \quad (2b)$$

334 In equations (2a-b),  $p$  is the ratio of the pressure level at which the W-vector is computed and  
 335 1000 hPa,  $\phi$  is the latitude,  $\lambda$  is the longitude,  $u$  and  $v$  are the zonal and meridional climatological  
 336 wind speeds, respectively,  $|u|$  is the climatological mean wind speed, and  $\psi'$  is the streamfunction  
 337 anomaly.

338

339 Variability in the ST, and perhaps to a lesser extent the SIT, is directly related to the SMB,  
 340 which can be expressed as

341 
$$SMB = P - Q_{sfc} - M - Q_{snow} - D \quad (3)$$

342 where  $P$  is the precipitation rate (mostly snowfall),  $Q_{sfc}$  is the surface evaporation/sublimation  
 343 rate,  $M$  is the surface melt and runoff rate,  $Q_{snow}$  is the blowing snow sublimation rate, and  $D$  is  
 344 the blowing snow divergence rate term, all with units of mm w.e.  $hr^{-1}$ . Blowing snow refers to  
 345 unconsolidated snow moved horizontally across the ice surface by winds above a certain threshold  
 346 speed (Massom et al., 2001). As detailed in Francis et al. (2023), the  $P$  and  $M$  terms are directly  
 347 extracted from ERA-5, for which the reanalysis values are in close agreement with satellite-derived  
 348 estimates over Antarctica, while the remaining three ( $Q_{sfc}$ ,  $Q_{snow}$ ,  $D$ ) are calculated using  
 349 parameterization schemes, described in Supplement Section S4. The hourly PWRF output is also  
 350 used to estimate the SMB for the 11-16 July 2022 case study, with  $M$  given by the decrease in ST  
 351 when the air temperature is above freezing after accounting for the other processes. Positive values  
 352 of SMB indicate an accumulation of snowfall at the site, while negative values represent a  
 353 reduction due to melting, sublimation or wind erosion processes, or a combination of the three. It  
 354 is also important to note that, following the convention of Dery and Yau (2002) adopted by Francis  
 355 et al. (2023), positive values of  $Q_{sfc}$  indicate deposition while negative values indicate  
 356 sublimation. For  $Q_{snow}$ , on the other hand, positive values indicate sublimation and negative  
 357 values indicate deposition.

358

359 Foehn effects, which play an important role in the SMB (e.g., Kuipers Munneke et al., 2017;  
 360 Francis et al., 2023), are identified using the methodology proposed by Francis et al. (2023). If, at  
 361 a given grid-point and hourly timestamp, the 2-m temperature exceeds its 60<sup>th</sup> percentile, the 2-m  
 362 relative humidity drops below its 30<sup>th</sup> percentile, and the 10-m wind speed exceeds its 60<sup>th</sup>  
 363 percentile, Foehn effects occur. The percentiles are grid-point dependent and are extracted for the  
 364 period 1979-2021. Monthly hourly thresholds are used for the 2-m temperature to account for the  
 365 annual cycle, while for the relative humidity and wind speed they are extracted for the full period.

366 **3. Sea-Ice and Snow Thickness Variability**

367 In Figs. 3a-b, the derived values of ST and SIT from 8 July to 30 November 2022 at the Khalifa  
368 SIMBA site on fast ice off Mawson Station are plotted. The uncertainty, which is estimated to be  
369 7% for ST and 2% for SIT (Liao et al., 2018), is highlighted by the blue shading. The SIT exhibits  
370 a gradual increase starting on 8 July, peaking at 1.14-1.16 m from 19-24 October, followed by a  
371 steady decline to 0.06-0.10 m at the end of November. These values are comparable to those  
372 estimated for this region and time of year using satellite-derived products, which are typically in  
373 the range 0.50-1.50 m (Kacimi and Kwok, 2020). The ST on top of the ice, on the other hand,  
374 exhibits pronounced day-to-day variations as high as 0.08 m, peaking in mid-August to early  
375 September, and with values not exceeding 0.10 m from mid-September to the end of November.  
376 These values are also in the range of those derived from satellite altimeter data for that coastal  
377 region (Kacimi and Kwok, 2020).

378

379 In order to explore whether atmospheric forcing could have played a role in the observed  
380 variability in SIT and ST, the local SMB is estimated around the Khalifa SIMBA site on fast ice  
381 off Mawson Station using ERA-5 data (Figs. 3c-d). An analysis of Figs. 2 and 3 reveals that the  
382 SIT appears to be mostly driven by the growth (increase in SIT) and melting (decrease in SIT) at  
383 the ice bottom which, on top of the oceanic heat flux (Heil et al., 1996; Haas, 2017), depends on  
384 the conductive heat flux driven by the atmospheric forcing. The annual SIT decrease that initiates  
385 in late October coincides with the time when the air temperature climbs above 265 K (Fig. 2a; Fig.  
386 3e) and there is increased solar insolation (note the strong diurnal variation in air temperature in  
387 Fig. 3e) at the site. On the other hand, a comparison of the ST observations and the SMB estimated  
388 from ERA-5 (equation 3) reveals a good correspondence between the two (cf. Figs. 3b with 3c-d).  
389 In particular, instances of positive SMB values (based on ERA-5) are typically associated with and  
390 followed by an increase in the measured ST at the site (e.g., in early July, mid-August, early and  
391 mid-October and mid-November), while negative SMB values from ERA-5 are accompanied by a  
392 decrease in the observed ST (e.g., in late July-early August and in late September-early October).  
393 Besides precipitation (snowfall) events, which can lead to an increase in ST by up to 0.06 m, Foehn  
394 effects also modulate the ST. These correspond to episodes when the wind direction is offshore  
395 (typically southerly to southeasterly), with an increase in wind speed and air temperature and a  
396 decrease in relative humidity. Foehn timestamps, identified following the methodology proposed  
397 by Francis et al. (2023) described in section 2.4, are shaded in purple in Fig. 3d. Several of these  
398 occurrences are seen during the study period, such as in mid-July, early August, mid-September  
399 and late October, leading to a reduction in ST of up to 0.08 m in a day (cf. Figs. 3b-f). This is not  
400 surprising, as the Khalifa SIMBA site on fast ice off Mawson Station is exposed to katabatic winds  
401 flowing seaward off the interior plateau (Dare and Budd, 2001), which experience adiabatic  
402 compression as they descend towards coastal areas. If the air temperature, relative humidity, and  
403 wind speed meet the criteria detailed in section 2.4, Foehn effects occur. Blowing snow, albeit less  
404 frequently, also affects the variability of ST: e.g., at the beginning of August, there is a 0.08 m  
405 decrease in ST during a blowing snow sublimation episode ( $Q_{snow}$  reaches 0.25 mm w.e.  $hr^{-1}$ )

406 followed by a Foehn event (Figs. 3b-f). Blowing snow divergence,  $D$ , on the other hand, plays a  
407 much-reduced role in the SMB, being of a larger magnitude during the passage of the AR on 14  
408 July that brought wind speeds in excess of  $30 \text{ m s}^{-1}$  (Figs. 3b-f). Surface melting is unlikely to be  
409 a major driver of ST, as evidenced by the zero values of  $M$  during the measurement period (Fig.  
410 3d). This is because during July-November 2022, the surface and air temperatures at the site  
411 remained below freezing (Figs. 2a and 3e).

412

413 Figs. 3g-l zoom-in during 11-16 July, when an AR impacted the site. The  $0.02 \text{ m}$  variations in  
414 SIT during 15-16 July, Fig. 3g, are within the uncertainty range and hence can be ascribed to the  
415 uncertainties in the methodology used for its estimation. The changes in ST, Fig. 3h, on the other  
416 hand, can be linked to atmospheric forcing (cf. Figs. 3i-j). On 14 July, heavy precipitation ( $>2 \text{ mm}$   
417  $\text{w.e. hr}^{-1}$ ) and strong easterly to southeasterly winds ( $> 30 \text{ m s}^{-1}$ ) occurred in association with the  
418 AR, with a steady increase in air temperature from around  $245 \text{ K}$  on 13 July to  $256 \text{ K}$  at the  
419 beginning of 15 July (Figs. 3k-l). On the following day, Foehn effects occurred, Fig. 3j, as in line  
420 with the decrease in relative humidity from  $\sim 83\%$  to  $60\%$ , the increase in wind speed from  $12$  to  
421  $28 \text{ m s}^{-1}$  with a shift from an easterly ( $96^\circ$ ) to a southeasterly ( $156^\circ$ ) direction, and a further  $4 \text{ K}$   
422 increase in air temperature, Figs. 3k-l. The negative  $Q_{sfc}$ , which indicates surface sublimation,  
423 plays a major role in the SMB during Foehn periods, Figs. 3i-j, in line with Francis et al. (2023).  
424 The  $0.02 \text{ m}$  drop in ST from 15 to 16 July, Fig. 3h, can be attributed to Foehn effects, while the  
425 absence of an increase in ST during the AR may be explained by the strong winds (Fig. 3l) that  
426 blow the snow away and prevent it from accumulating at the instrument's location (note the  
427 positive blowing snow divergence,  $D$ , during the precipitation event, Fig. 3j). In fact, it has been  
428 reported that strong katabatic winds have blown the snow away as quickly as it falls on nearshore  
429 fast ice near the Mawson (Dare and Budd, 2001) and Syowa (Kawamura et al., 1995) stations,  
430 resulting in very low accumulation close to the coast. ERA-5 predicts some precipitation on 16  
431 July, Fig. 3i, even though at much reduced levels compared to 14 July. However, the fact that the  
432 wind speed is much lower on this day, dropping below  $2 \text{ m s}^{-1}$  (Fig. 3l), allows for snow  
433 accumulation at the Khalifa SIMBA site on fast ice off Mawson Station, which contributes to the  
434 observed  $0.04 \text{ m}$  increase in ST. It is important to note that a longer measurement period that  
435 comprises multiple AR passages would be needed for a robust link between ARs and their effects  
436 on ST and SIT to be established.

437

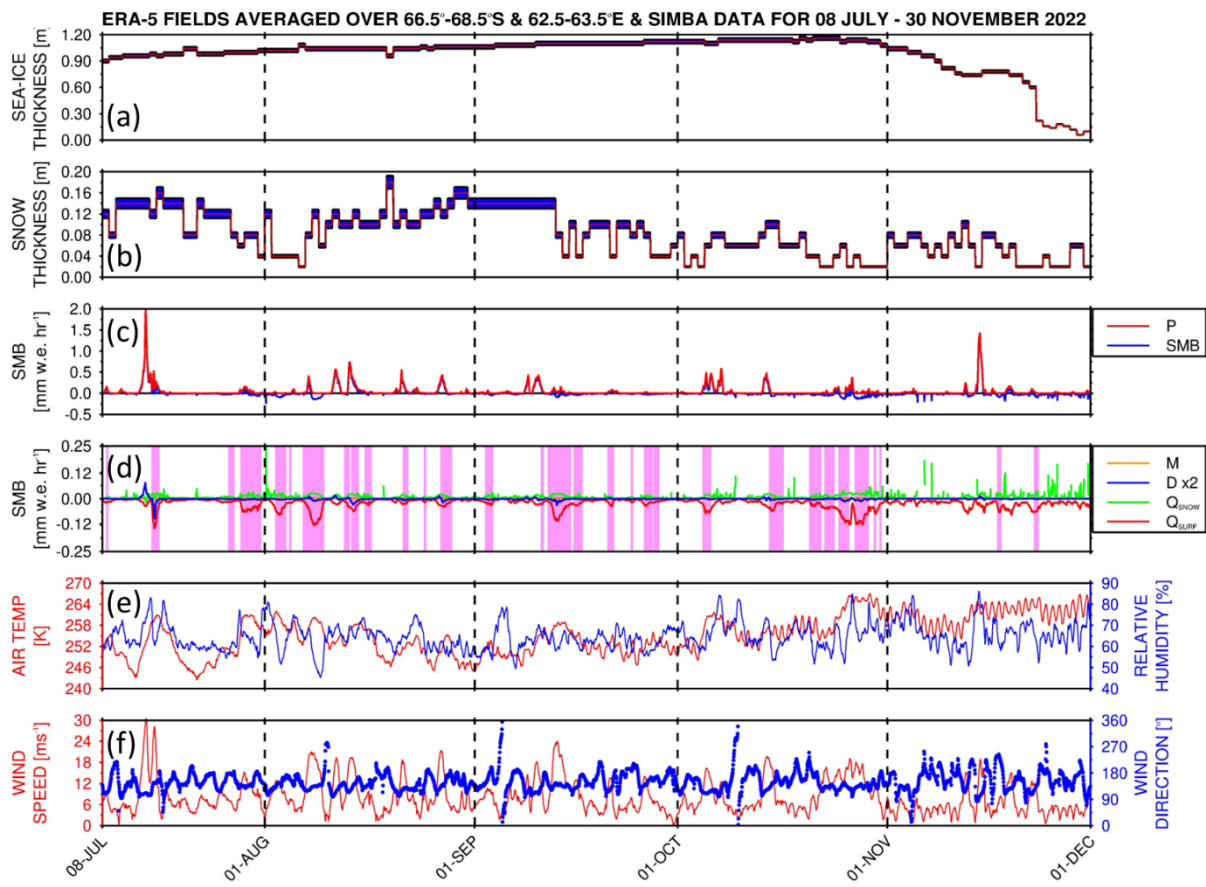
438 Figure 4a gives the Pook Blocking Index, defined in Equation S6, for the study period. It  
439 reveals a few blocking events east of the site around  $120^\circ\text{E}$  in late July-early August,  $150^\circ\text{E}$  in mid-  
440 September, and around the Dateline in mid- to late-November. Zoomed-in plots around the time  
441 of the Mawson AR passage highlight the occurrence of blocking around the Dateline and  $60^\circ\text{W}$   
442 (Fig. 4d). The latter actually coincided with the passage of three consecutive ARs west of the  
443 Antarctic Peninsula (Fig. 4f), with the air temperature climbing above freezing (Fig. 4e). Wille et  
444 al. (2024c) and MacLennan et al. (2023) stressed that the occurrence of blocking can lead to the  
445 development of an “AR family” (or multi-AR) event, with the counterclockwise flow around the

446 high-pressure and subsequent poleward advection of warm and moist low-latitude air masses  
 447 leading to a marked rise in temperature. This is evident in particular around 120°E in late July-  
 448 early August and mid-September, and around 150°E in late November (Figs. 4a-c). At the Khalifa  
 449 SIMBA site on fast ice off Mawson Station, on the other hand, blocking did not occur, as evidenced  
 450 by the small values of the Pook Blocking Index (Fig. 4a). During the case study in mid-July (Figs.  
 451 4d-f), the presence of a ridge east of Mawson led to a second warm and moist air intrusion around  
 452 70°-90°E on 16 July. The passage of the AR at Mawson on 14 July coincided with an increase in  
 453 air temperature by more than 15 K in a couple of days (Fig. 4e), consistent with the observed rise  
 454 in air temperature of ~18 K at the site (Fig. 2a).

455

456 The results in Figure 4 highlight the role of atmospheric dynamics in modulating the ST at the  
 457 Khalifa SIMBA site on fast ice off Mawson Station, with the SIT largely controlled by the oceanic  
 458 and conductive heat flux and the seasonal variability in the incoming solar radiation.

459



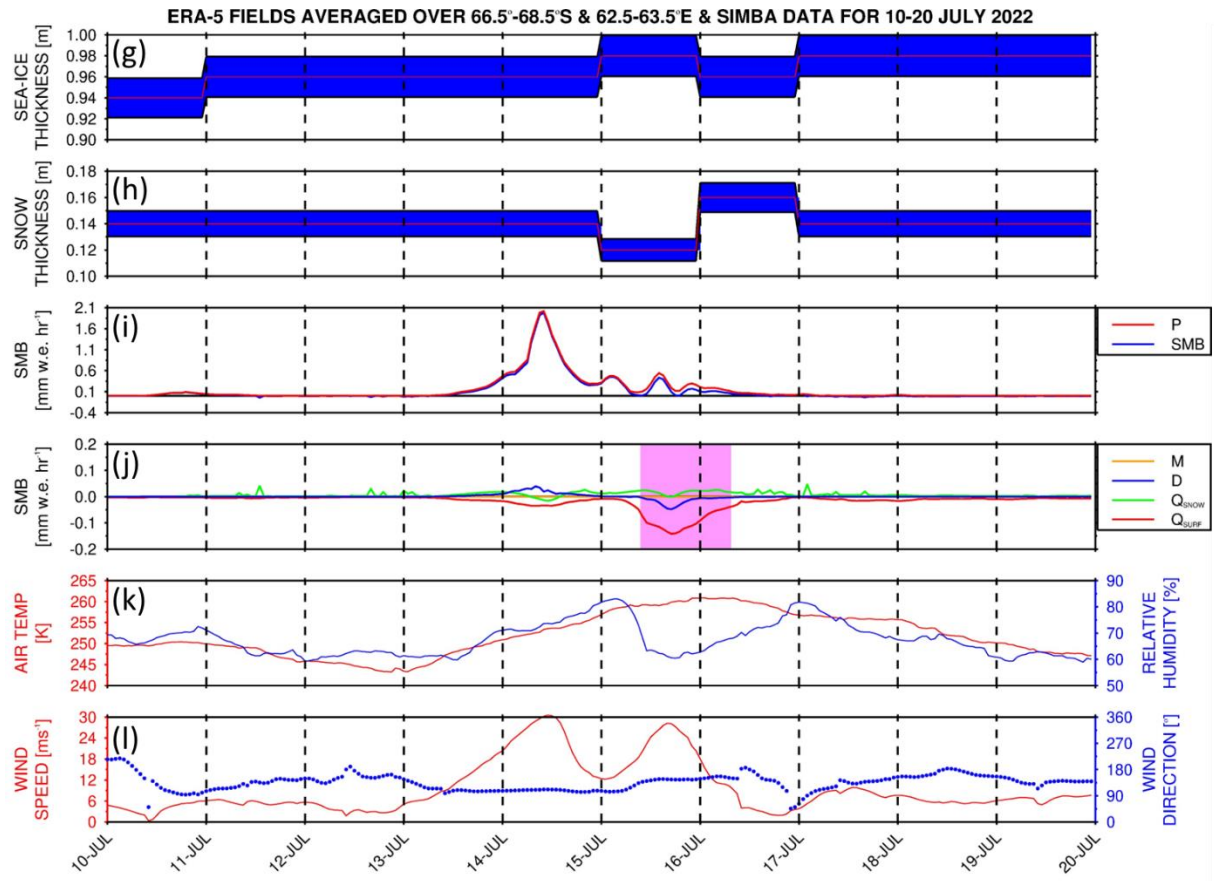


**Figure 3: Surface Mass Balance and SIMBA Observations:** (a) ST and (b) SIT from the SIMBA measurements for the period 08 July to 30 November 2022. The red line shows the observed values while the blue shading gives the uncertainty, which is estimated as 7% for ST and 2% for SIT (Liao et al., 2018). (c)-(d) give the hourly SMB terms ( $\text{mm w.e. hr}^{-1}$ ) from ERA-5 averaged over the domain  $66.5^{\circ}$ - $68.5^{\circ}\text{S}$  and  $62.5^{\circ}$ - $63.5^{\circ}\text{E}$ . Shown is the SMB (blue) and precipitation (red;  $P$ ) in (c), and the snowmelt (orange;  $M$ ), surface sublimation (red;  $Q_{sfc}$ ), blowing snow sublimation (green;  $Q_{snow}$ ), and blowing snow divergence (blue;  $D$ ) in (d). No snowmelt occurred during the measurement period, and the  $D$  term is multiplied by two for visualization purposes. The purple shading in (d) highlights hourly timestamps when Foehn effects occurred anywhere in the domain. (e)-(f) give the reanalysis' domain averaged hourly air temperature (red; K) and relative humidity (blue; %) in (e), and horizontal wind speed (red;  $\text{m s}^{-1}$ ) and direction (blue;  $^{\circ}$ ) in (f). (g)-(l) are as (a)-(f) but for 10-20 July 2022. No scaling is applied to the  $D$  term in (j).

460  
461  
462  
463  
464  
465  
466  
467  
468

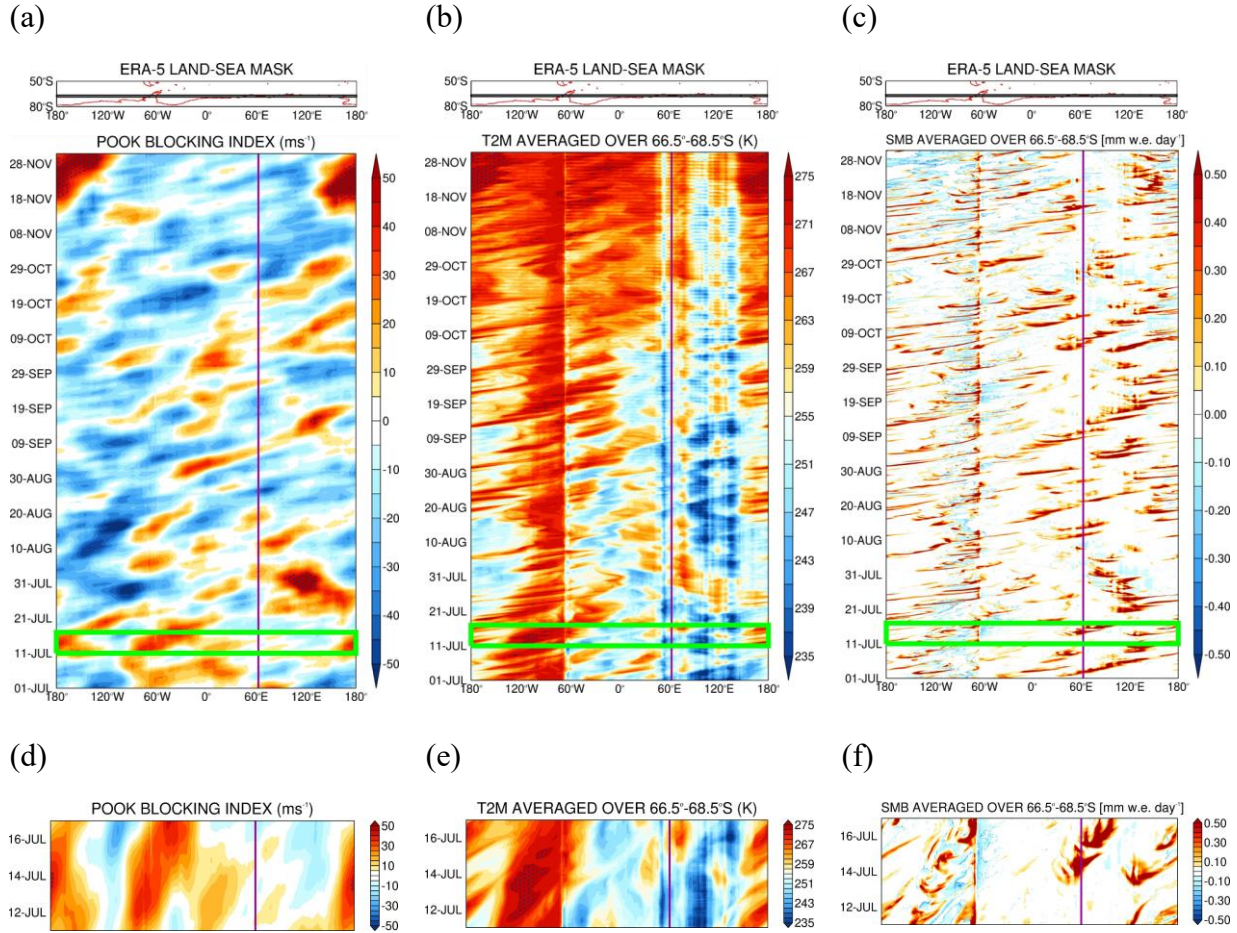


**Figure 4: Atmospheric dynamics and thermodynamics during the Observational Period:** (a) Pook blocking index ( $\text{m s}^{-1}$ ) for July-November 2022. The vertical purple line gives the approximate longitude of the measuring site. Regions where the index exceeds  $40 \text{ m s}^{-1}$ , an indication of a high degree of blocking, are stippled. The green rectangles indicate the period when an AR impacted the site 11-16 July. Above the Hovmöller plot, the land-sea mask as seen by ERA-5 is plotted in red and the averaging region is highlighted with a black rectangle. (b) and (c) are as (a) but for air temperature (K) and the SMB, defined in equation (3), respectively, averaged over  $68.5^{\circ}$ - $66.5^{\circ}$ S. The sharp transition in the temperature field around  $60^{\circ}$ W arises due to the presence of the Antarctic Peninsula (landmass), while the stipple in (b) indicates regions and times when the temperature is above freezing (273.15 K). (d)-(f) are as (a)-(c) but zooming in for 11-16 July 2022.

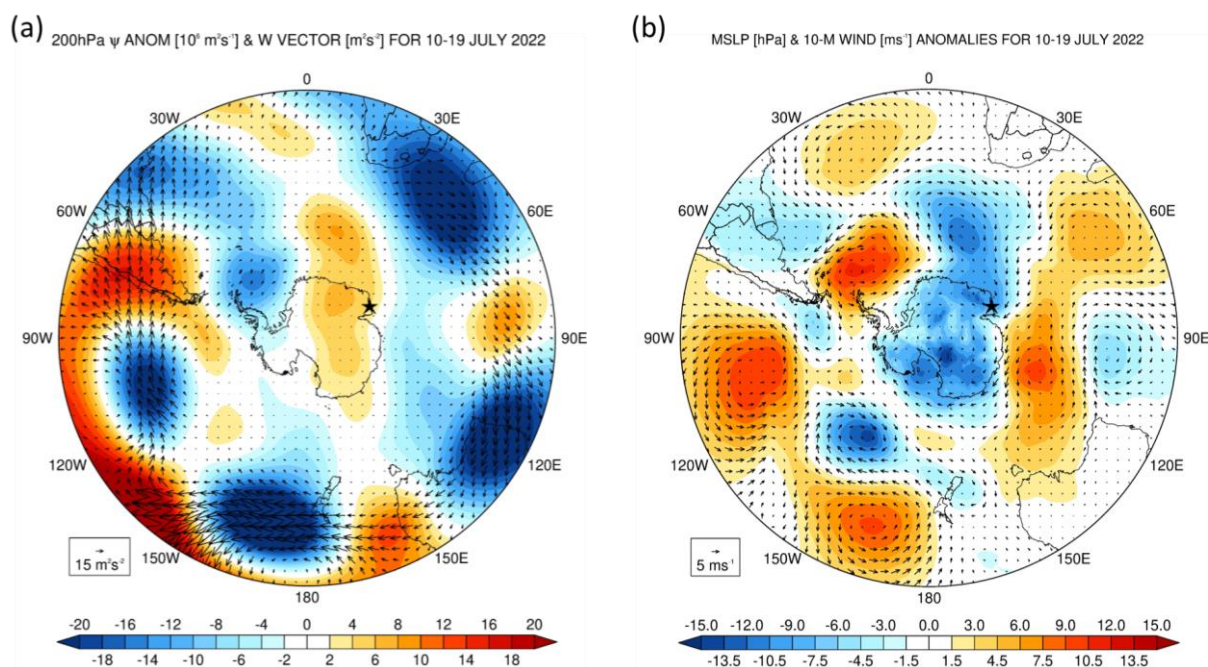
#### 469 4. Case Study: 11-16 July 2022

470 An AR impacted the site during July-November 2022 on 14 July. In Section 4.1, the large- and  
 471 regional-scale environment that promoted the development of the AR is investigated, while in  
 472 Section 4.2 the results of the PWRF simulations are discussed.

473 **4.1 Large-Scale Atmospheric Patterns**

474 The period 10-19 July 2022 is characterized by a strong wavenumber 3 pattern along the  
 475 Southern Hemisphere polar jet at about 60°S and a wavenumber 5 pattern along the subtropical jet  
 476 at about 30°S (Fig. 5a), projecting onto the positive phase of SAM (Fig. 5b). The stationary wave  
 477 activity flux vectors in Fig. 5a show little wave propagation from the tropics into the Southern  
 478 Hemisphere mid-latitudes, with a prevailing zonal propagation within the wavenumber #5 pattern.  
 479 This is also evidenced by the strong westerly flow around Antarctica (Fig. 5d). One of the reasons  
 480 for the positive SAM is the La Niña that was taking place at the time, the third consecutive La  
 481 Niña year after the 2018-2019 El Niño (NOAA/NWS, 2024), as La Niña events typically project  
 482 onto the positive SAM pattern (Fogt et al., 2011).

483



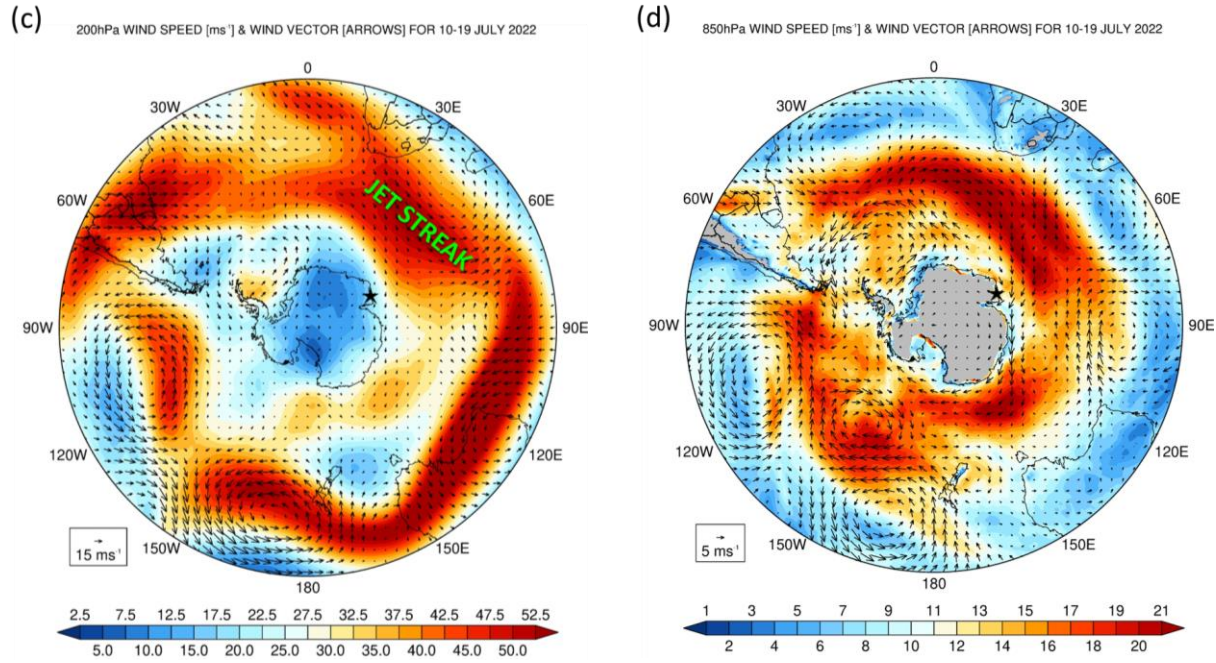


**Figure 5: Large-Scale Circulation during 10-19 July 2022:** (a) 200 hPa stream-function anomalies (shading;  $10^6 \text{ m}^2 \text{s}^{-1}$ ), with respect to the hourly 1979-2021 climatology, and stationary W vectors (Takaya and Nakamura, 2001; equations (2a) and (2b); arrows;  $\text{m}^2 \text{s}^{-2}$ ) averaged over 10-19 July 2022. (b) Sea-level pressure (shading; hPa) and 10-m wind vectors (arrows;  $\text{m s}^{-1}$ ) anomalies for the same period. (c) and (d) show the 200 hPa and 850 hPa wind speed (shading;  $\text{m s}^{-1}$ ) and vectors (arrows) averaged over the same period. The jet streak referred to in the text is highlighted in (c). In all panels, the star gives the location of Mawson Station ( $67.5912^\circ\text{S}$ ,  $62.8563^\circ\text{E}$ ).

484

485

486 North of Mawson Station, a pressure dipole is present around  $40^\circ$ - $65^\circ\text{S}$  (Fig. 5b), with a ridge to  
487 the east and a trough to the west. This pattern favours the poleward propagation of warm and moist  
488 low-latitude air into the Khalifa SIMBA site on fast ice off the Mawson Station in East Antarctica,  
489 and is conducive to the development of ARs (Francis et al., 2022b; Gorodetskaya et al., 2023).  
490 The interaction between the subtropical jet and polar jet led to the development of a jet streak (Fig.  
491 5c), a localized maximum in the strength of the flow. The low pressure associated with the AR  
492 (Fig. 5a) is located to the south of the jet entrance, in an area favourable for cyclogenesis (Wallace  
493 and Hobbs, 2006). Despite its slow eastward movement and anomalous high strength, the  
494 meridional extent of the ridge from East Antarctica to southeastern Madagascar may explain why  
495 it is not detected by the Pook Blocking Index, Fig. 4a and Equation S6, as the westerly flow at  $35^\circ$ -  
496  $40^\circ\text{S}$  and  $65^\circ$ - $70^\circ\text{S}$  is also weaker. The AR that developed on 14 July 2022 is particularly  
497 remarkable, extending from the southwestern Indian Ocean into the Southern Ocean and East  
498 Antarctica, and having its primary origin in South America (Figs. 6a-b). The wavetrain extending  
499 from South America to the southeastern Pacific Ocean comprises a ridge over southern parts of  
500 Chile and Argentina, and a low over northern Argentina to the west of South Atlantic subtropical  
501 high (Figs. S1b, S1d and S1f). The pressure gradient between the latter two systems leads to a  
502 strengthening of the South American low-level jet (Marengo et al., 2004; Montini et al., 2019),

503 which advects moisture from equatorial South America into the subtropics and helps to feed  
504 convection east of the Andes (Figs. S1a, S1c, and S1e). The moist outflow coming out of South  
505 America and the latent heat release from the convection strengthen the low pressure to the  
506 southwest of South Africa that is tracking southeastwards, and promote the development of the  
507 AR that impacted the Khalifa SIMBA site on fast ice off Mawson Station on 14 July. After a first  
508 landfall on 14 July around Mawson Station, Fig. 6a, the AR made a second landfall around 75°-  
509 90°E, Fig. 6b, impacting a wide swath of East Antarctica from about 45°E to 100°E. Here, the air  
510 temperature anomalies generally exceeded 10 K, with some parts of East Antarctica having near-  
511 surface temperatures in the top 1% of the 1979-2021 climatological distribution (Fig. 6d). The IVT  
512 at 06 UTC on 14 July exceeds  $156 \text{ kg m}^{-1} \text{ s}^{-1}$  around the Khalifa SIMBA site on fast ice off Mawson  
513 Station and  $800 \text{ kg m}^{-1} \text{ s}^{-1}$  further north along the AR (Fig. 6b), with the hourly IVT on this day  
514 being in the top 0.5% of the climatological distribution (Fig. 6c), an attestation to the extreme  
515 nature of this event. A back-trajectory analysis performed with HYSPLIT forced with ERA-5 data  
516 revealed tropical and subtropical moisture sources contributed to the 14 July 2022 AR (Fig. S2a).  
517 While at lower levels the moisture came from the Southern Ocean, with specific humidity values  
518 generally below  $2 \text{ g kg}^{-1}$  and air temperatures generally below freezing, at 2250 m it originated in  
519 the subtropics just south of South Africa with specific humidity values in excess of  $6 \text{ g kg}^{-1}$  and  
520 air temperatures around 280-290 K (Figs. S2b-e). The latter air mass ascended from roughly 200  
521 m to 2250 m just north of Mawson Station when it encountered the colder and drier airflow (Fig.  
522 S2a). Several studies report on ARs impacting Antarctica being fed by subtropical moisture, such  
523 as the February 2011 (Terpstra et al., 2021) and the November-December 2018 (Gorodetskaya et  
524 al., 2020) ARs over East Antarctica, and the February 2022 AR over the Antarctica Peninsula  
525 (Gorodetskaya et al., 2023).

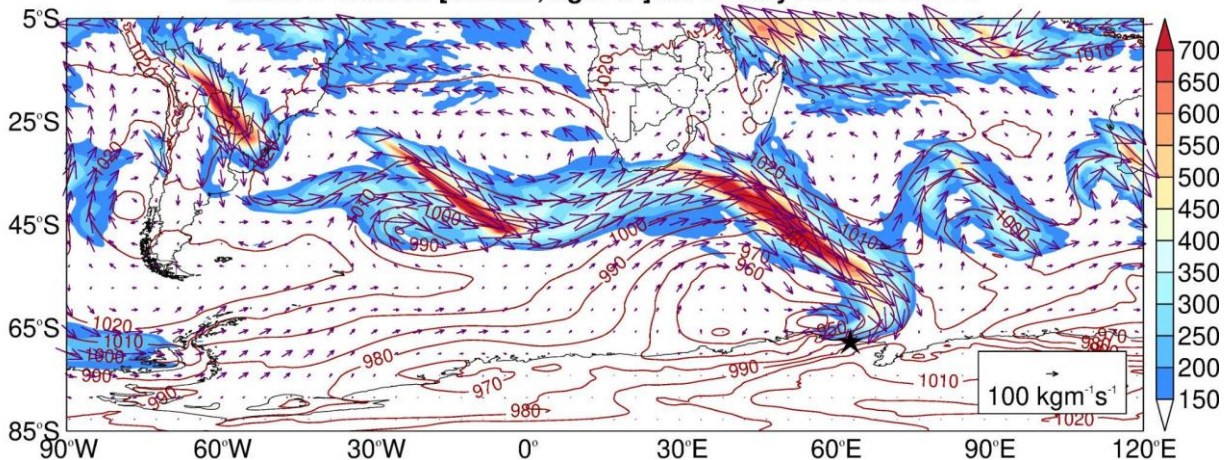
526  
527 The AR and attendant cyclone also had an important effect on the sea ice in the region. As seen in  
528 Figs. S3a-b, there was a considerable reduction in SIE from 12 to 16 July both around coastal  
529 Antarctica and upstream, with an open-ocean polynya developing well northwest of Mawson  
530 Station around  $65^{\circ}\text{S}, 45^{\circ}\text{E}$  on 14 July and disappearing on 22 July. The role of ARs and the surface  
531 divergent flow associated with the attendant cyclone in opening up polynyas has been reported at  
532 multiple sites around Antarctica (Francis et al. 2019, 2020). The low-pressure system northwest of  
533 Mawson reached a minimum value of 944 hPa on 12 July over the Southern Ocean, with the  
534 secondary low that formed on 14 July reaching 933 hPa on this day at 06 UTC just off the Khalifa  
535 SIMBA site on fast ice off Mawson Station (Fig. 6a), and deepening further to 931 hPa late on 15  
536 July just to the northeast of the site (Fig. 6b). These systems are stronger than those that played a  
537 role in the opening up of the Weddell Sea Polynya in September 1973 and 2017 (Francis et al.,  
538 2020), and the Maud Rise Polynya in September 2017 (Francis et al., 2019). The sea-ice vectors  
539 in Figs. S3c-d show an equatorward movement north of Mawson Station from 12-14 July (prior to  
540 the event) at speeds in excess of  $40 \text{ km day}^{-1}$ , and a southward movement from 14-16 July (post  
541 event) at speeds in excess of  $20 \text{ km day}^{-1}$ . These sea-ice drift velocities, which are associated with  
542 the changing wind field in response to the shift in the position of the mid-latitude weather systems

543 in the region (Figs. 6a-b, 6d and 7) are higher than those observed in the western Ross Sea in late  
 544 April 2017 (Fonseca et al., 2023), and comparable to those estimated in the region in September  
 545 2017 (Francis et al., 2019).

546

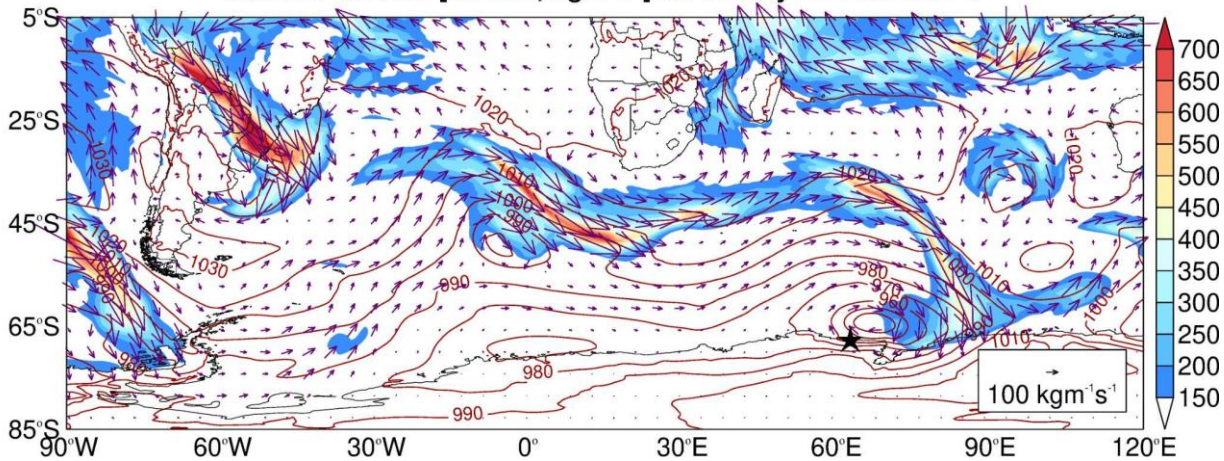
(a)

**Sea-Level Pressure [contours; hPa], IVT Magnitude [shading;  $\text{kgm}^{-1}\text{s}^{-1}$ ]  
 and IVT Vectors [arrows;  $\text{kgm}^{-1}\text{s}^{-1}$ ] on 14 July 2022 at 06UTC**



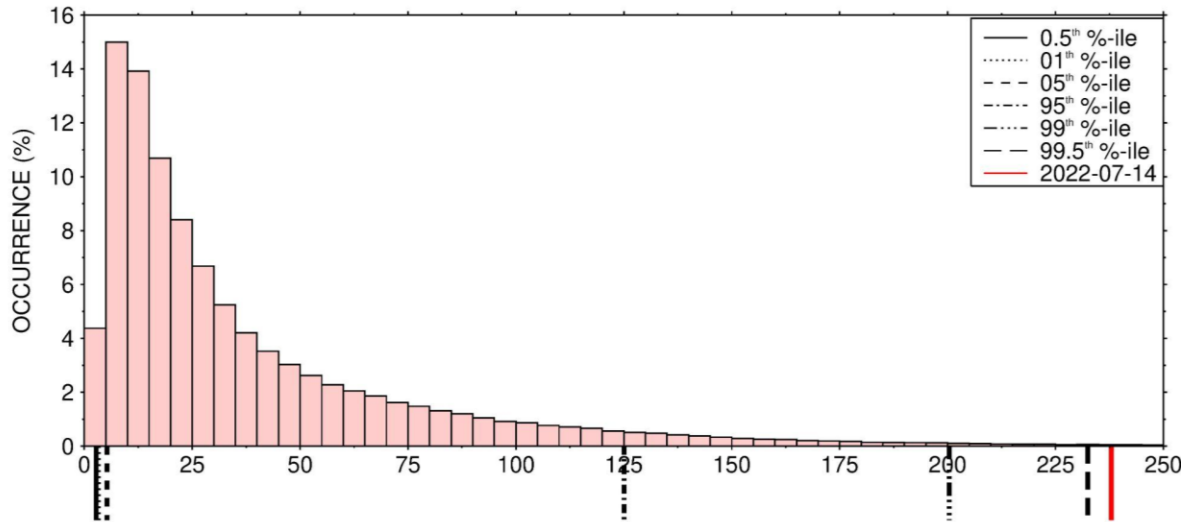
(b)

**Sea-Level Pressure [contours; hPa], IVT Magnitude [shading;  $\text{kgm}^{-1}\text{s}^{-1}$ ]  
 and IVT Vectors [arrows;  $\text{kgm}^{-1}\text{s}^{-1}$ ] on 15 July 2022 at 15UTC**



(c)

MAXIMUM OF HOURLY IVT ( $\text{kg m}^{-1} \text{s}^{-1}$ ) OVER 68.5°-66.5°S & 62.5°-63.5°E FOR 1979-2021



(d)

AIR TEMPERATURE [K] & 10-M WIND [ $\text{ms}^{-1}$ ] ANOMALIES ON 16-JUL-2022 @ 00UTC

GREEN STIPPLE: AIR TEMPERATURE IN TOP 1% OF 1979-2021 CLIMATOLOGY

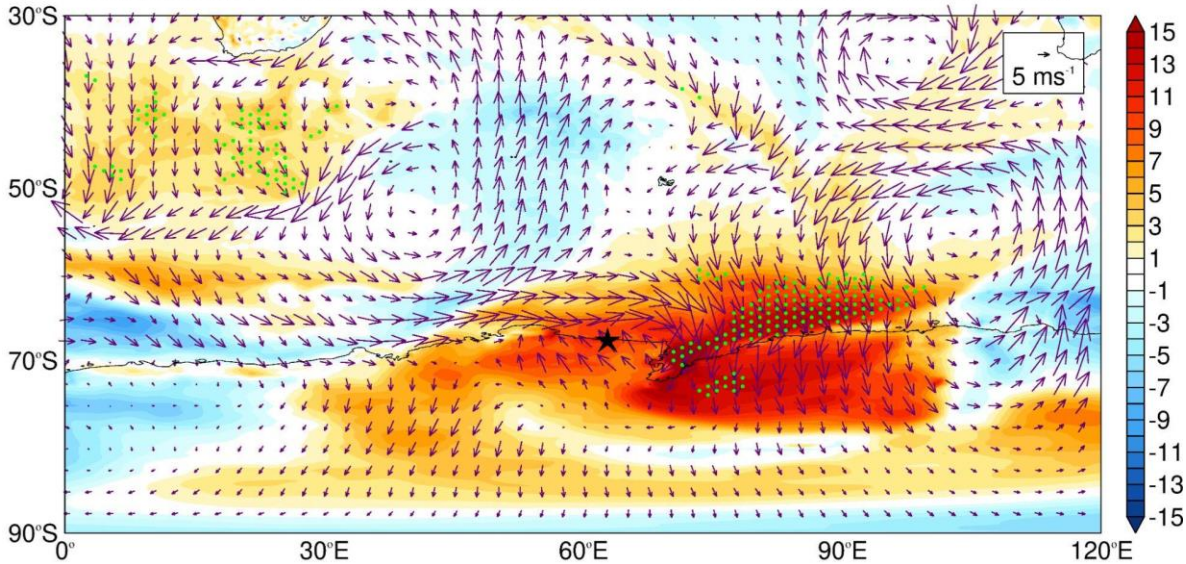


**Figure 6: Atmospheric River on 14 July 2022:** (a) Sea-level pressure (contours; every 10 hPa), Integrated Vapour Transport (IVT) magnitude (shading;  $\text{kg m}^{-1} \text{s}^{-1}$ ) and vectors (arrows;  $\text{kg m}^{-1} \text{s}^{-1}$ ) on (a) 14 July 2022 at 06 UTC and (b) 15 July 2022 at 15 UTC from ERA-5. The star gives the location of the Mawson station. (c) Histogram of the maximum hourly IVT around the Mawson station (68.5°-66.5°S and 62.5°-63.5°E) for 1979-2021. The solid, dotted, dashed, dotted-dashed, dashed-dotted-dotted and long dashed lines give the 0.5<sup>th</sup>, 1<sup>st</sup>, 5<sup>th</sup>, 95<sup>th</sup>, 99<sup>th</sup> and 99.5<sup>th</sup> percentiles, respectively, while the red line indicates the maximum hourly values on 14 July 2022. (d) air temperature (shading; K) and 10-m wind vectors (arrows;  $\text{ms}^{-1}$ ) anomalies with respect to 1979-2021 climatology on 16 July 2022 at 00 UTC. The green stipple indicates regions where the air temperatures are in the top 1% of the 1979-2021 climatological distribution.

548 Figures 5-6 provide a summary of the weather conditions during 10-19 July 2022, with Fig. 6  
549 focusing on the AR event that impacted Mawson Station on 14 July. In order to gain insight into  
550 this AR event, it is important to assess the temporal evolution of the atmospheric circulation prior  
551 to and during the event itself. This is achieved in Fig. 7, which shows multiple fields from 13 July  
552 at 06 UTC to 15 July at 18 UTC. At 06 UTC on 13 July (Fig. 7a), a broad low-pressure system is  
553 centered northwest of the site, coincident with a TPV (highlighted in the figure), with a ridge to its  
554 east. The TPV helps the surface low to intensify, together with the jet streak at upper levels (Fig.  
555 5c), with the central pressure dropping to around 944 hPa on 12 July at 12 UTC. The pressure  
556 dipole promotes the southward advection of a warmer and moist low-latitude air mass into the  
557 Southern Ocean, as noted by the hatching that highlights regions where the IVT exceeds  $250 \text{ kg m}^{-1} \text{ s}^{-1}$ .  
558 A secondary low, which develops later on 13 July (highlighted in Fig. 7c, also noted by the  
559 additional sea-level pressure contour), is not co-located with a TPV. Instead, the secondary low is  
560 driven by the interaction of the warm and moist air mass from the west and northwest around the  
561 low pressure with that from the northeast around the ridge. Closer to the Antarctic coast, the  
562 aforementioned low-level convergence is reinforced by the drier and colder katabatic flow blowing  
563 from the continent. The maximum Eady growth rate, a measure of baroclinicity (Hoskins and  
564 Valdes, 1990), at 850 hPa exceeded  $3 \text{ day}^{-1}$  on 14 July (not shown), indicating a highly baroclinic  
565 environment.

566

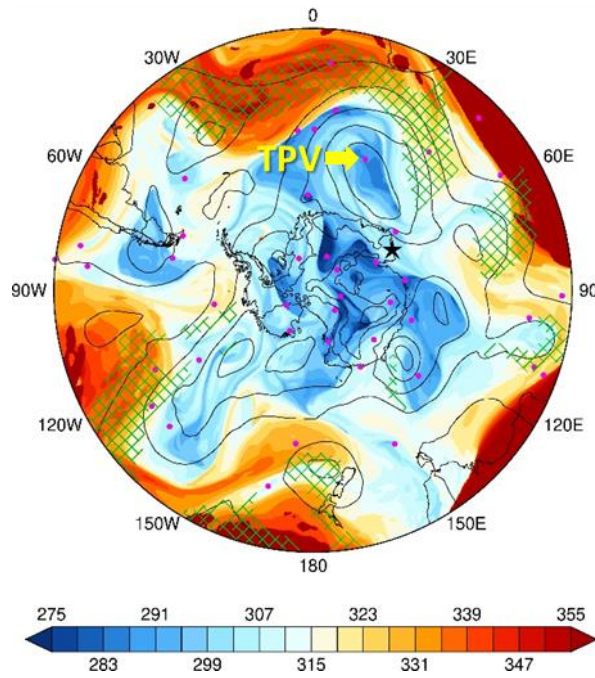
567 Figures 7b-d show cyclonic Rossby wave breaking, with the secondary low exhibiting little  
568 eastward movement owing to the presence of a ridge to the east (Figs. 6a-b), and instead shifting  
569 southwards towards Antarctica. The incursion of the higher low-latitude potential temperature  
570 values into East Antarctica (Figs. 7b-d) is consistent with the warmer (Fig. 6d) and more moist  
571 (Figs. 6a-c) conditions in the region. The warm and moist air intrusion shifted eastwards from 14  
572 to 15 July (Figs. 7c-d) and penetrated deeper into East Antarctica on 15-16 July (Figs. 7d and 6d),  
573 with air temperatures more than 15 K above climatology in some parts (Fig. 6d). Fig. 7 shows more  
574 than one episode of intrusion of low-latitude air masses into Antarctica. For example, on 14-16  
575 July a warm and moist air intrusion reached the Antarctic Peninsula (Figs. 7c-d). Such occurrences  
576 are more common in an amplified pattern and can be aided by TPVs that act to strengthen the  
577 attendant cyclone (Wille et al., 2024c).

578

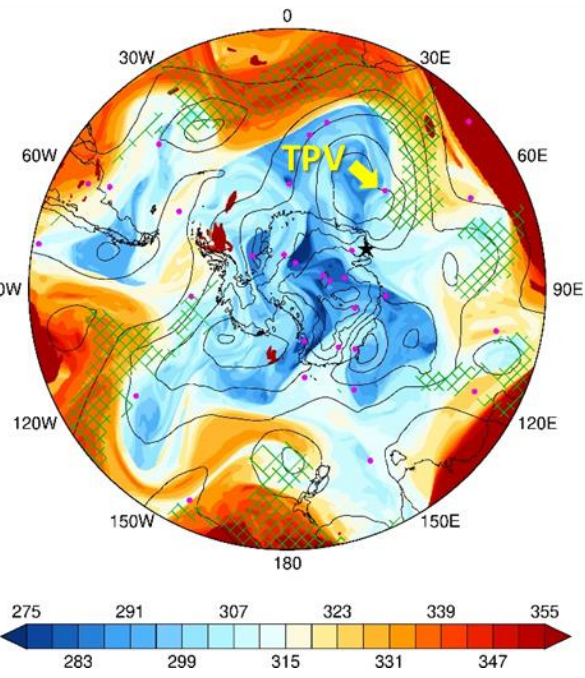
(a)

(b)

13 JULY 2022 @ 06 UTC

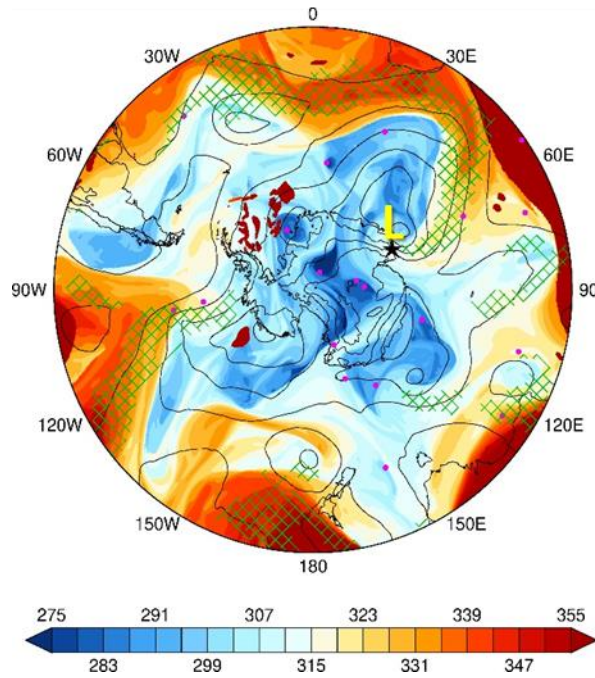


13 JULY 2022 @ 18 UTC



(c)

14 JULY 2022 @ 06 UTC



(d)

15 JULY 2022 @ 18 UTC

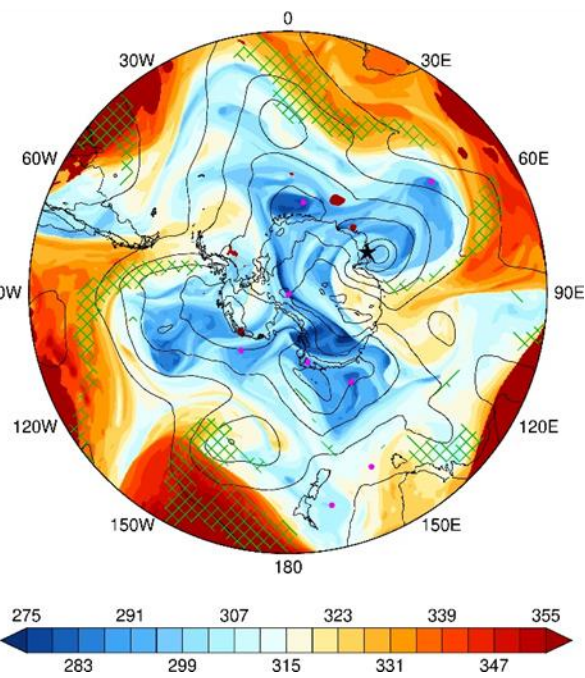


**Figure 7: Evolution of Atmospheric State during 13-15 July 2022:** Potential temperature ( $\theta$ ; shading; K) on the dynamical tropopause ( $PV = -2$  PVU), sea-level pressure (black contours; every 15 hPa starting at 900 hPa) and integrated vapour transport (IVT; hatching if  $> 250 \text{ kg m}^{-1} \text{ s}^{-1}$ ) on 13 July at (a) 06 UTC

and (b) 18 UTC, (c) 14 July at 06 UTC, and (d) 15 July at 18 UTC. The purple dots indicate the location of tropopause polar vortices (TPV) at the respective times. The TPV and the secondary low pressure discussed in the text are highlighted in panels (a)-(b) and (c), respectively.

579

## 580 4.2 PolarWRF Simulation

581 In this subsection, the focus is on the modeling experiments. In Section 4.2.1, the PWRF  
582 predictions are evaluated against *in-situ* measurements at the five stations in East Antarctica given  
583 in Fig. 1d, while in Section 4.2.2 the emphasis is on the additional insight the higher-resolution  
584 model data gives on the mid-July 2022 AR event.

### 585 4.2.1 Evaluation of PolarWRF

586 The PWRF simulations for 11-16 July 2022 are evaluated against *in-situ* meteorological  
587 observations at the Mawson, Syowa, Relay, Davis and Casey stations, in addition to surface  
588 radiation fields at Syowa Station. Fig. 8 shows the time-series of hourly data for the Mawson and  
589 Syowa stations, with the corresponding time series for the other two stations given in Fig. S4. A  
590 quantitative assessment of the model performance for all stations and variables is presented in  
591 Table 3.

592

593 PWRF simulates the weather conditions well at the Mawson (Figs. 8a-f), Syowa (Figs. 8g-1  
594 and S4a-f), Relay (Fig. S4g-l), Davis (Fig. S4m-r) and Casey (Fig. S4s-x) stations for 11-16 July  
595 2022. In particular, the observed variability in sea-level pressure is well replicated, with the model  
596 correctly capturing the time of passage and strength of the secondary cyclone on 14-15 July at  
597 Mawson (Figs. 7c-d; Fig. 8c) and on 15 July at the Davis (Fig. 7d; Fig. S4p) Stations. Moreover,  
598 the warmer, more moist and windier conditions on 12-14 July at Syowa Station (Figs. S4a-c and  
599 S4f), on 14-15 July at Mawson (Fig. 8a-c and 8e) and Relay (Fig. S4g-i and S4l) Stations, and on  
600 15-16 July at Davis (Fig. S4m-o and S4r) and Casey (Fig. S4s-u and S4x) Stations are predicted  
601 by the model. Also, the model captures the increase in the downward long-wave radiation flux by  
602 up to  $80 \text{ W m}^{-2}$  at Syowa Station (Fig. 8k) in association with the warm and moist air intrusion on  
603 13-14 July. An inspection of Table 3 reveals that, and except mainly for the air temperature and  
604 surface pressure, the normalized bias  $\mu$  is smaller than 0.5, indicating the biases can be regarded  
605 as not significant, while the normalized error variance  $\alpha$  does not exceed 1 for all fields and stations  
606 (except for the wind vector at the higher-elevation Relay and coastal Davis Stations), indicating  
607 that the PWRF predictions can be regarded as trustful. The performance of PWRF for this event is  
608 comparable to that for the McMurdo Station in early January 2016 (Hines et al., 2019), for West  
609 Antarctica in early to mid-January 2019 (Bromwich et al., 2022), and for the Antarctic Peninsula  
610 for May-June 2019 and January 2020 (Matejka et al., 2021). This reflects the improvements made  
611 to PWRF by the model developers, with the aim of optimizing its performance and skill over  
612 Antarctica (e.g., Hines et al., 2021).

613

614 A closer inspection of Figs. 8 and S4 and Table 3 reveals some discrepancies in the PWRF  
615 predictions. For example, at Syowa Station, the model has a tendency to over-predict the air  
616 temperature by  $\sim$ 1-3 K. This may explain the overestimation of the upward longwave radiation  
617 flux by about  $14.3 \text{ W m}^{-2}$  (Fig. 8l), which can also arise from an overprediction of the observed  
618 surface emissivity. The downward longwave radiation flu (Fig. 8k), on the other hand, is  
619 underestimated by roughly  $7.7 \text{ W m}^{-2}$ , likely related to the reduced atmospheric moisture content  
620 in the model by about  $\sim 0.16 \text{ g kg}^{-1}$ . At all four coastal Antarctica stations, the predicted wind  
621 direction is generally shifted clockwise by  $45^\circ$ - $90^\circ$  compared to that observed (Figs. 8d, S4e, S4q  
622 and S4w), with this mismatch at times reaching  $180^\circ$  at the Relay Station (Fig. S4k) located on the  
623 Antarctic plateau more than 3,000 m above sea-level (Fig. 1d). This discrepancy can be attributed  
624 to an incorrect representation of the surface topography which exhibits a complex spatial  
625 heterogeneity in the region (Lea et al., 2024). Despite these issues, both the magnitude and  
626 variability of the observed wind speed are generally well represented by PWRF (Figs. 8e, S4f, S4l,  
627 S4r, and S4x). The more offshore wind direction at the coastal Antarctica stations reflect a stronger  
628 katabatic wind regime that acts to slow the poleward movement of the low-latitude air mass, which  
629 is consistent with the dry bias of up to  $0.2 \text{ g kg}^{-1}$ . The positive mixing ratio bias at the Relay Station  
630 occurs primarily on 15-16 July (Fig. S4h), and is associated with increased but still rather low  
631 (generally below  $0.1 \text{ g kg}^{-1}$ ) moisture levels advected from the interior of Antarctica. At all stations  
632 except Mawson, PWRF exhibits a warm bias (Figs. 8a, 8g, S4g, S4m, and S4s), with the near-  
633 surface wind speed being underestimated at Mawson (Fig. 8e) and overestimated at the other  
634 stations (Figs. S4f, S4l, S4r, and S4x). Together with the dry bias, this suggests a tendency for  
635 excessive boundary layer mixing in the model compared to observations, which has been reported  
636 in a number of PWRF studies (e.g., Wille et al. 2016, 2017; Vignon et al., 2019). An optimized  
637 PBL scheme, which at least partially corrects for the excessive mixing, and/or a more sophisticated  
638 land surface model that more accurately represents the boundary layer and surface processes, have  
639 to be considered to address the aforementioned biases. Despite this, PWRF captures the effects of  
640 the AR as seen in observations, most notably the increase in air temperature and water vapour  
641 mixing ratio, and the strengthening of the near-surface wind in particular at the more impacted  
642 Mawson (Figs. 8a-e) and Davis (Figs. S4m-r) stations.  
643

644 The SMB analysis performed using ERA-5 data is repeated using the hourly PWRF predictions.  
645 Figs. S5a-b give the observed SIT and ST measurements, while Figs. S5c-d show the different  
646 terms of the SMB as predicted by PWRF. The model gives a similar estimate of the components  
647 of the SMB with respect to the reanalysis dataset (cf. Figs. S5c-d with 3i-j), with the roughly 30%  
648 higher surface sublimation on 15 July arising from the drier ( $\sim$ 10% lower relative humidity; cf.  
649 Figs. S5e with 3k) and windier ( $\sim$ 10% higher wind speed; cf. Figs. S5f with 3l) near-surface  
650 conditions in the model. The fact that ERA-5 captures Foehn effects at this site and for this event,  
651 suggests that it can be used for the wider analysis of Foehn events around East Antarctica, as has  
652 been done over West Antarctica (Francis et al., 2023) and the Antarctica Peninsula (Laffin et al.,  
653 2021). The up to  $\sim$ 2 mm w.e.  $\text{hr}^{-1}$  precipitation rate (Figs. S5c and 3i),  $\sim$ 5 K air temperature increase  
654 (Fig. S5e and 3k), and  $30 \text{ m s}^{-1}$  wind speeds (Figs. S5f and 3l) associated with the passage of the

655 AR on 14 July are simulated by PWRF, with the cold bias in the model also seen in comparison  
656 with *in-situ* measurements at Mawson Station (Table 3).

657  
658 Fig. 8f shows a comparison of the observed and simulated snow depth at the Khalifa SIMBA site  
659 on fast ice off Mawson Station. The ST in PWRF is initialized to zero, and hence the discrepancy  
660 with respect to the observed values during 11-13 July (the observed ST is equal to 0.14 m during  
661 10-14 July). PWRF predicts around 0.24 m of snowfall in association with the passage of the AR  
662 on 14 July, and the weaker wind speeds in the model, at times by more than  $20 \text{ m s}^{-1}$ , likely allow  
663 for snow to accumulate at the site instead of it being blown away by the wind. The model fails to  
664 capture the observed decrease of 0.02 m in ST on 15 July in response to Foehn effects, which can  
665 be attributed to less favourable conditions for Foehn events in the model (e.g., the wind speed is  
666 lower by as much as  $20 \text{ m s}^{-1}$ , Fig. 8e, with generally cooler air temperatures, Fig. 8a). A higher  
667 spatial resolution of at least 1 km would probably be needed for a more accurate simulation of the  
668 interaction of the AR with the complex Antarctic topography including the Foehn effects (Gilbert  
669 et al., 2025). The increase in ST on 16 July due to snowfall is simulated by PWRF, even though  
670 its magnitude is underestimated by the model (0.01 m in PWRF as opposed to 0.04 m in  
671 observations), possibly because of the drier environment brought on by a more offshore wind  
672 direction (Figs. 8b, 8d-e, and S5e-f). It is important to stress that the discrepancies between the  
673 observed and modelled ST can also be tied to deficiencies in the LSM. In particular, the Noah  
674 LSM used in this study only considers a single snow layer and has a simplified representation of  
675 snow accumulation, sublimation, and melting processes (Lim et al., 2022). In contrast, the more  
676 sophisticated Noah LSM with multiparameterization options (Noah-MP), also available in PWRF  
677 and that features user-defined parameters, includes up to three snow layers, represents the  
678 percolation, retention, and refreezing of meltwater within the snowpack, and accounts for snow  
679 metamorphism and compaction (Niu et al., 2011). Recent work has shown that it gives a superior  
680 performance with respect to the Noah LSM over Antarctica with respect to the 2-m temperature  
681 and 10-m wind speed forecasts (Xue et al., 2022). An extension of this work would be to consider  
682 the Noah-MP and explore its effects on the ST predictions.

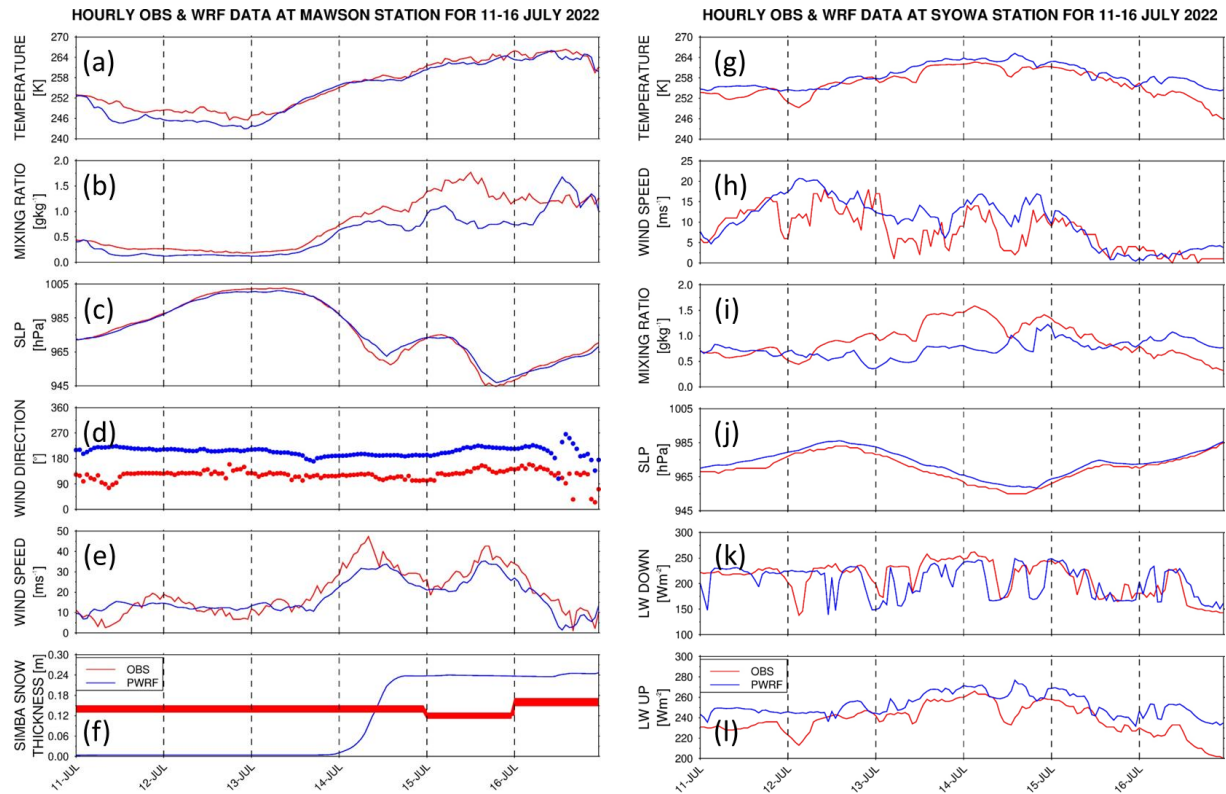
683  
684 Besides ground-based observations, sounding data are available at the Mawson, Syowa, Davis,  
685 and Casey stations every 12 h and can be compared with the hourly PWRF predictions (Figs. S6  
686 and S7). The model captures the timing of the arrival of the warm and moist air mass at Mawson  
687 on 14-15 July, as evidenced by the higher values of  $\theta_E$  (270-280 K; Figs. S6a and S6e) and relative  
688 humidity (60-90%; Figs. S6b and S6f). However, the katabatic wind flow is stronger in the model  
689 as seen by the offshore wind direction (Fig. S6h) and drier conditions (Figs. S6b and S6f), and also  
690 evident in the ground-based observations (Figs. 8d and 8b), with a strong low-level jet (mostly  
691 below 700 hPa) on 14 and 16 July (Fig. S6g). At Syowa, the PWRF and observed profiles are in  
692 closer agreement than at the Mawson Station (cf. Figs. S6a-h with S6i-p). Here, the main  
693 discrepancy between the observed and modelled profiles is the dry bias (Figs. S6j and S6n), which  
694 is more pronounced on 13-14 July, and is also evident in the near-surface data (Fig. 8i). The arrival

695 of the low-latitude air mass at Davis on 15 July is seen in both the PWRF and observed profiles  
 696 (Figs. S7a-h), with a less pronounced katabatic regime in the model compared to that at Mawson  
 697 Station (cf. Figs. S6e-h with S7e-h). At Casey (Figs. S7i-p), PWRF simulates the more moist  
 698 conditions on 14 July and the drier conditions on 15-16 July. The analysis of the sounding profiles  
 699 reveals, however, that PWRF tends to overestimate the strength of the katabatic flow over coastal  
 700 East Antarctica during 11-16 July. Vignon et al. (2019) attribute such overestimates to more stable  
 701 boundary layers over the Antarctic Plateau and, to a lesser extent, steeper synoptic land-ocean  
 702 pressure gradients in the model.

703

704 The results in Figs. 8, S4-S7, and Table 3 reveal a reasonably good PWRF performance in the  
 705 study area for the period 11-16 July 2022. In the next subsection, the model simulations are used  
 706 to gain further insight into the dynamics of the 14 July AR event.

707



708 **Figure 8: Evaluation of PolarWRF against ground-based observations:** Hourly (a) air temperature  
 709 ( $^{\circ}\text{C}$ ), (b) water vapour mixing ratio ( $\text{g kg}^{-1}$ ), (c) sea-level pressure (SLP; hPa), and horizontal wind (d)  
 710 direction ( $^{\circ}$ ) and (e) speed ( $\text{m s}^{-1}$ ) from observations (red) and the PWRF simulation (blue) for 11-16 July  
 711 2022 at Mawson Station. (f) shows the daily observed (red) and hourly PWRF-predicted (blue) ST (m)  
 712 at the Khalifa SIMBA site on fast ice off Mawson Station, the former with the estimated 7% uncertainty.  
 713 (g)-(l) is as (a)-(f) but for the hourly air temperature (K), horizontal wind speed ( $\text{m s}^{-1}$ ), water vapour  
 714 mixing ratio ( $\text{g kg}^{-1}$ ), sea-level pressure (SLP; hPa), and surface downward and upward longwave  
 715 radiation fluxes ( $\text{W m}^{-2}$ ), respectively at Syowa Station. The wind fields at Syowa Station are shown in  
 716 Figs. S4e-f. The location of the stations is given in Fig. 1d.

717

Variable	Station	Bias	$\mu$	$\rho$	$\eta$	$\alpha$
Air Temperature	Mawson	-1.42 K	-0.92	0.98	~1.0	0.02
	Syowa	2.15 K	1.08	0.87	0.98	0.14
	Relay	2.51 K	0.65	0.90	~1.0	0.10
	Davis	3.11 K	1.30	0.98	0.97	0.05
	Casey	2.66 K	1.22	0.75	0.97	0.27
Water Vapour Mixing Ratio	Mawson	-0.21 g kg <sup>-1</sup>	-0.82	0.86	0.98	0.16
	Syowa	-0.16 g kg <sup>-1</sup>	-0.45	0.05	0.82	0.96
	Relay	0.01 g kg <sup>-1</sup>	0.69	0.75	0.99	0.25
	Davis	-0.09 g kg <sup>-1</sup>	-0.28	0.97	0.94	0.08
	Casey	-0.02 g kg <sup>-1</sup>	-0.12	0.61	0.92	0.43
Wind Vector (Bias and $\mu$ are for wind speed)	Mawson	-2.39 m s <sup>-1</sup>	-0.48	0.27	0.96	0.74
	Syowa	2.36 m s <sup>-1</sup>	0.61	0.39	~1.0	0.61
	Relay	2.02 m s <sup>-1</sup>	1.82	-0.60	~1.0	1.60
	Davis	1.40 m s <sup>-1</sup>	0.36	-0.30	0.99	1.29
	Casey	0.79 m s <sup>-1</sup>	0.24	0.08	0.98	0.93
Surface Pressure	Mawson	-3.78 hPa	-1.72	0.99	~1.0	0.01
	Syowa	3.08 hPa	2.35	0.99	~1.0	0.01
	Relay	2.53 hPa	3.16	0.99	0.99	0.02

	Davis	-0.74 hPa	-0.50	~1.0	~1.0	0.01
	Casey	-2.48 hPa	-2.16	~1.0	0.99	0.01
<b>Downward LW</b>	Syowa	-7.71 W m <sup>-2</sup>	-0.24	0.47	~1.0	0.53
<b>Upward LW</b>	Syowa	14.26 W m <sup>-2</sup>	1.54	0.79	0.95	0.25

710  
711  
712  
713  
714  
715  
716  
717  
718

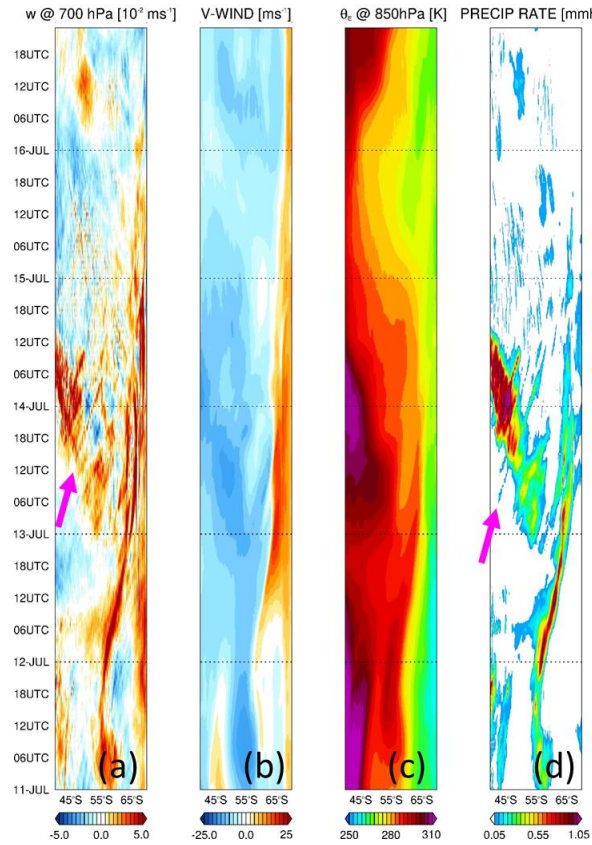
**Table 3: Verification diagnostics with respect to station data:** Bias, normalized bias ( $\mu$ ), correlation ( $\rho$ ), variance similarity ( $\eta$ ), and normalized error variance ( $\alpha$ ) for air temperature, water vapour mixing ratio, horizontal wind vector and sea-level pressure for Mawson, Syowa, Relay, Davis, and Casey Stations for 11-16 July 2022. For Syowa Station, the scores are also given for the surface downward and upward longwave radiation fluxes at the bottom of the table. The model values are those at the closest grid-point to the location of the station, and the evaluation is performed for hourly data. The correspondent time-series are given in Figs. 8 and S4.

## 719 4.2.2 Insights into the Dynamics and Effects of the AR

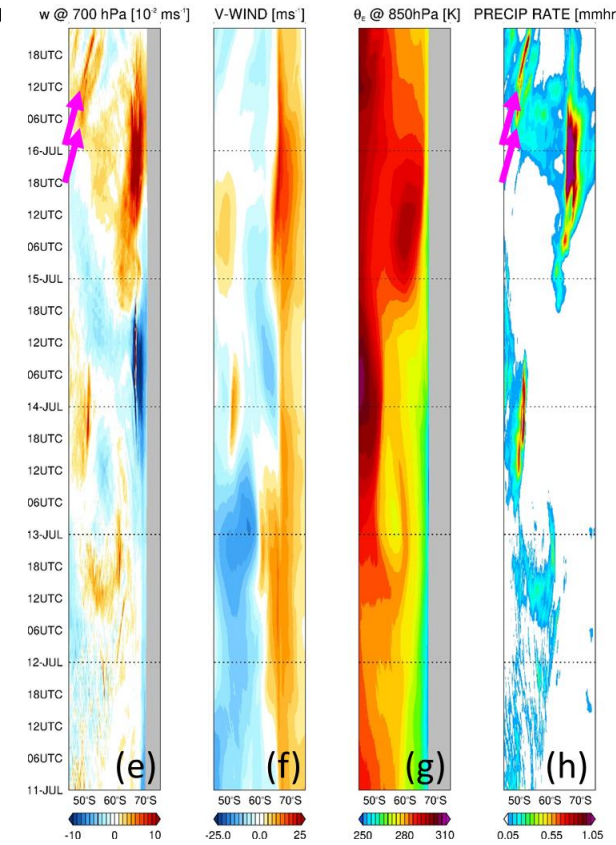
720 One of the motivations for implementing the high-resolution (2.5 km) innermost grid is to  
721 check for the presence of AR rapids (Box et al., 2023; Francis et al., 2024). Figs. 9a-d show a  
722 hovmoeller plot of the vertical velocity at 700 hPa, 10-m meridional wind speed, 850 hPa  
723 equivalent potential temperature ( $\theta_E$ ), and precipitation rate averaged over 40°-50°E, a latitude  
724 band that comprises the bulk of the AR (Figs. 6a, 7a-c and 9i). It reveals AR rapids, in particular  
725 one on 13-14 July between 40°-60°S (pink arrows in Figs. 9a and 9d), which is embedded within  
726 the AR, as seen on 13 July at 12 UTC when it is located at 40°-50°S (Fig. 9i). No AR rapids are  
727 seen in the vertical profiles at the coastal Antarctic stations (Figs. S6 and S7), suggesting they are  
728 confined to the Southern Ocean. The linear structure propagating from ~55°S late on 11 July to  
729 65°S early on 13 July does not correspond to an AR rapid. Instead, the heavy precipitation ( $>1$  mm  
730 hr<sup>-1</sup>; Fig. 9d) arises from the interaction of the low-latitude air mass with the katabatic wind regime  
731 originating from the Antarctic Plateau, as it is placed at the interface between the two flows (cf.  
732 Figs. 9a-b with 9d). The low-level convergence of these two air masses can be seen in Fig. 9i  
733 around 65°S. The katabatic flow is characterized by southerly winds (Fig. 9b) and low  $\theta_E$  values  
734 (260-270 K, compared to 290-300 K for the low-latitude air mass; Fig. 9c), extending from the  
735 Antarctic Plateau to the Southern Ocean. Figs. 9e-h are as Figs. 9a-d but the fields are averaged  
736 over 85°-95°E. The low-latitude air mass reaches this part of East Antarctica on 15-16 July, when  
737 precipitation rates exceed 1.8 mm w.e. hr<sup>-1</sup>. The maximum precipitation rate in coastal Antarctica  
738 and averaged over 85°-95°E is about 66% higher than that averaged over 40°-50°E (1.81 vs. 1.09  
739 mm w.e. hr<sup>-1</sup>). This can be explained by (1) the higher moisture levels (maximum longitudinally-  
740 averaged  $\theta_E$  values of 297.9 K vs. 289.7 K), as the low-latitude air mass penetrates further  
741 polewards due to a more favourable synoptic pressure pattern, and (2) a stronger katabatic flow

742 off the Antarctic Plateau (maximum longitudinally-averaged meridional wind speed of  $22\text{ m s}^{-1}$  vs.  
743  $19\text{ m s}^{-1}$ ). Around  $45^{\circ}$ - $55^{\circ}\text{S}$  on 16 July, AR rapids are present in the plots averaged over  $85^{\circ}$ - $95^{\circ}\text{E}$   
744 (pink arrows in Figs. 9e and 9h), when the low-level air intrusion was in the area (Fig. 9j). The  
745 fact that these structures have been identified in modelling products in the Southern Ocean in this  
746 study, around Greenland in Box et al. (2023), and in the Middle East in Francis et al. (2024),  
747 stresses the need for high spatial and temporal resolution three-dimensional radar observations  
748 along the ARs to check whether they actually exist or are just model artefacts.  
749

HOVMOELLER PLOTS AVERAGED OVER 40°-50°E FOR 11-16 JULY 2022



HOVMOELLER PLOTS AVERAGED OVER 85°-95°E FOR 11-16 JULY 2022



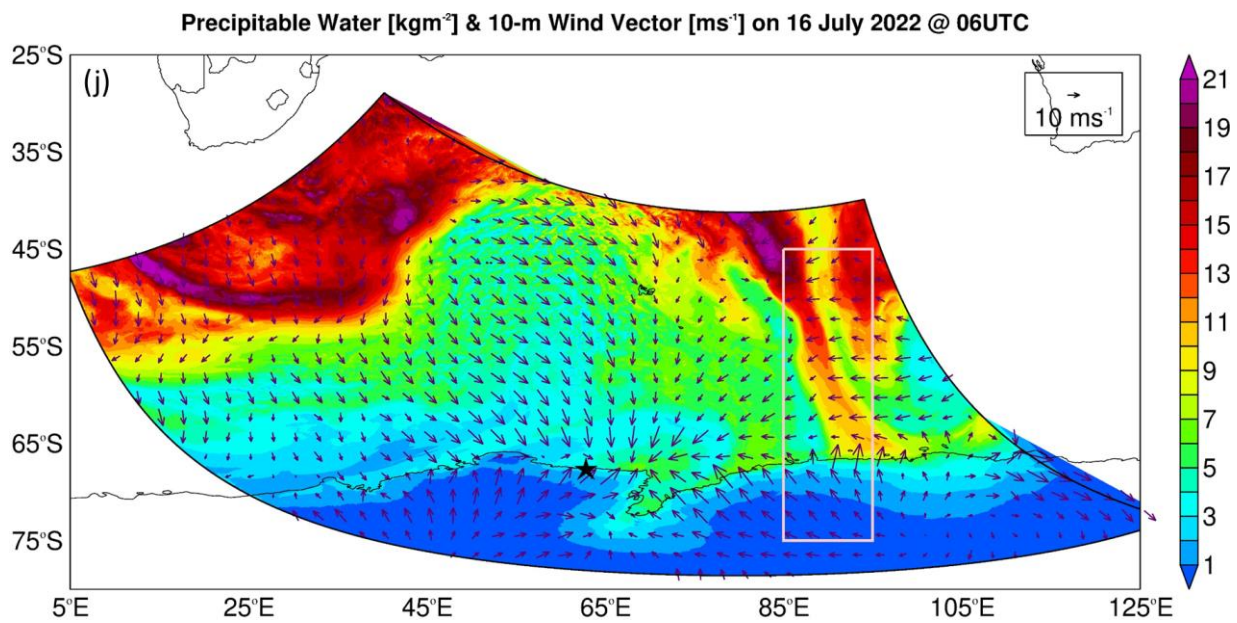
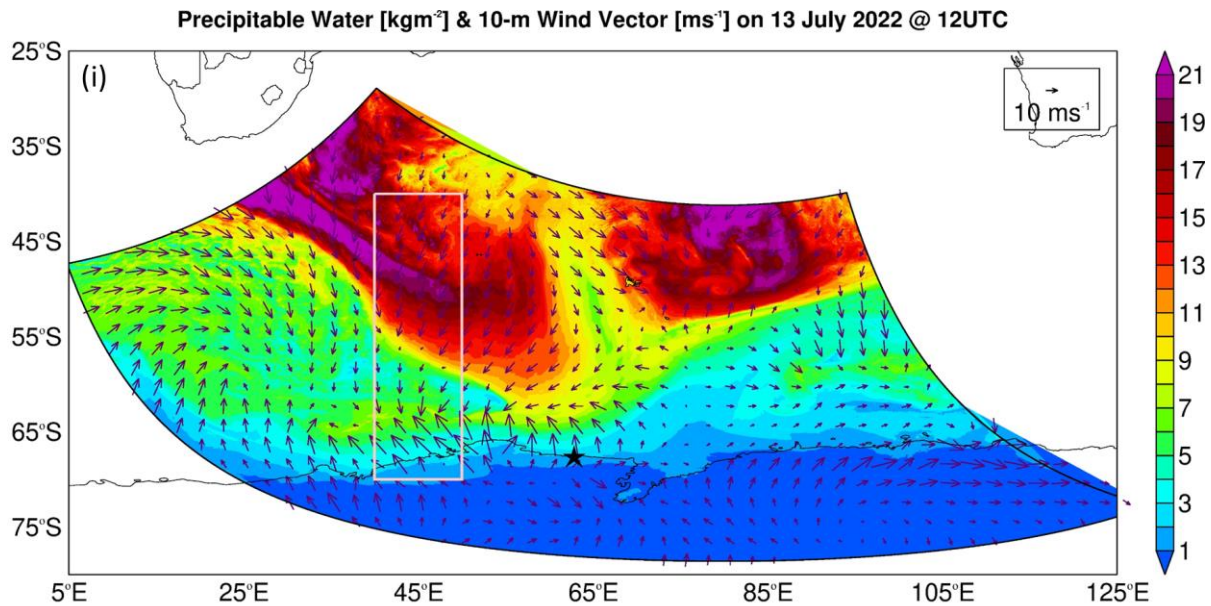


**Figure 9: Hovmoeller Plots:** Hovmoeller of hourly (a) 700 hPa vertical velocity ( $10^2 \text{ m s}^{-1}$ ), (b) 10-m meridional wind speed ( $\text{m s}^{-1}$ ), (c) 850hPa equivalent potential temperature ( $\theta_E$ ; K), and (d) precipitation rate ( $\text{mm hr}^{-1}$ ) for 11-16 July 2022 averaged over  $40^\circ$ - $50^\circ\text{E}$ . The pink arrows highlight AR rapids. (e)-(h) are as (a)-(d) but averaged over  $85^\circ$ - $95^\circ\text{E}$ . The grey shading in (e) and (g) highlights latitudes for which the 700 hPa and 850 hPa pressure levels, respectively, are below topography. (i) Precipitable water (shading;  $\text{kg m}^{-2}$ ) and 10-m wind vector (arrows;  $\text{m s}^{-1}$ ) at 12 UTC on 13 July. The star indicates the

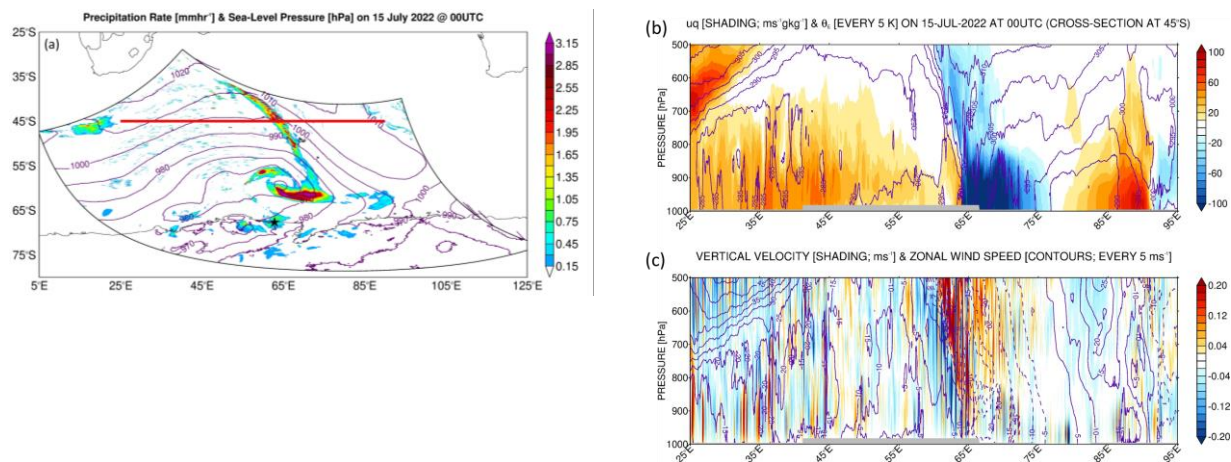
location of Mawson Station. The fields given in (a)-(d) are averaged over the longitude band of the pink box ( $40^{\circ}$ - $50^{\circ}$ E) and plotted over its latitude range. (j) is as (i) but at 06 UTC on 16 July, with the pink box also giving the latitude range over which the fields in (e)-(h) are plotted, and its longitude band ( $85^{\circ}$ - $95^{\circ}$ E) that used for averaging to generate the hovmoeller plots.

750

751 On top of surface evaporation from the subtropics (Fig. S2), the convergence of the flow  
 752 around the low-pressure system to the west and the ridge to the east helped feed the AR and  
 753 associated warm and moist air mass (Fig. 7). This can be seen in Figs. 10a-c. The zonal moisture  
 754 transport in Fig. 10b highlights the convergence of the westerly flow at  $5$ - $10$   $m\ s^{-1}$  associated with  
 755  $\theta$  values of  $290$ - $295$  K, with the easterly flow around the high with zonal wind speeds of  $20$ - $25$   $m$   
 756  $s^{-1}$  and  $\theta_E$  values of  $300$ - $305$  K, as this air mass comes directly from the tropics. At about  $65^{\circ}$ E,  
 757 where the AR is located (Fig. 10a), the vertical velocity peaks in the mid-troposphere around  $600$ -  
 758  $800$  hPa with speeds up to  $0.3\ m\ s^{-1}$  (Fig. 10c). The vertical structure of the updrafts, with a peak in  
 759 the low-to-mid troposphere, and the updraft speeds are comparable to the AR rapids reported by  
 760 Box et al. (2023) over Greenland on 14 September 2017. Precipitation rates in excess of  $3\ mm\ hr^{-1}$   
 761 are simulated by the model at 12 UTC on 14 July (Fig. 10d) and at 00 UTC on 15 July (Fig. 10a)  
 762 along the AR. As the moisture plume moved closer to the Antarctic coast, it interacted with the  
 763 katabatic wind regime. This is evident in Figs. 10e-f, with the colder, drier ( $\theta_E \sim 260$ - $265$  K) and  
 764 strong (meridional wind speeds in excess of  $45\ m\ s^{-1}$ ) airflow from Antarctica, which descends the  
 765 steep slopes with downward vertical velocities up to  $-0.6\ m\ s^{-1}$ , converging with the slower ( $35$ - $40$   
 766  $m\ s^{-1}$ ) and more moist ( $\theta_E \sim 275$ - $280$  K) flow from lower-latitudes with vertical velocities in the  
 767 bottom  $5$  km reaching  $+0.3\ m\ s^{-1}$ . This convergence led to precipitation rates in excess of  $3\ mm\ hr^{-1}$   
 768 around Mawson Station (Fig. 10d).

769 The results in Figs. 9 and 10 suggest that it can be difficult for ARs and associated warm and moist  
 770 air intrusions to reach this region of East Antarctica owing to the interaction with the strong  
 771 katabatic flow. This factor has been highlighted for other regions of East Antarctica (e.g., Terpstra  
 772 et al., 2021; Gehring et al., 2022).

773



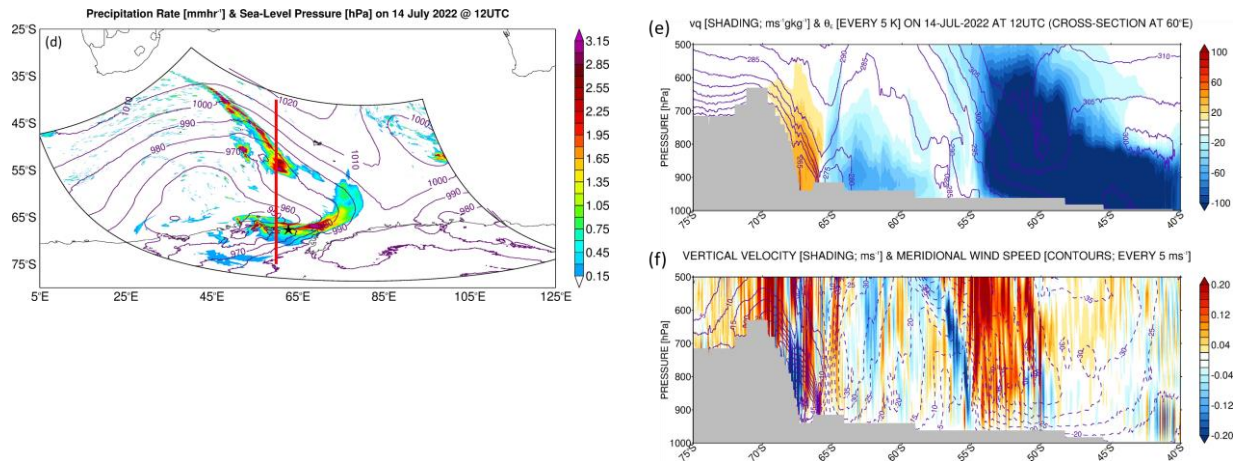


**Figure 10: Precipitation mechanisms in the Southern Ocean:** (a) Precipitation (shading;  $\text{mm hr}^{-1}$ ) and sea-level pressure (contours; hPa) at 00 UTC on 15 July 2022, from PWRF's 2.5 km grid. Vertical cross-section at 45°S, red line in (a), of (b) zonal mass transport (shading;  $\text{m s}^{-1} \text{g kg}^{-1}$ ) and equivalent potential temperature ( $\theta_E$ ; contours; every 5 K), and (c) vertical velocity (shading;  $10^{-2} \text{m s}^{-1}$ ) and zonal wind speed (contours; every 5  $\text{m s}^{-1}$ ), at the same time. Regions below the orography are shaded in grey. (d)-(f) are as (a)-(c) but at 12 UTC on 14 July. The cross-section is at 60°E, with the meridional mass transport and meridional wind speed in (e) and (f) plotted instead of their zonal counterparts, respectively.

774

775 **5. Discussion and Conclusions**

776 Sea ice is a critically important component of the climate system, modulating atmosphere-  
777 ocean interactions and ultimately the global climate (Raphael et al., 2011; Goosse et al., 2023).  
778 Antarctic SIE has abruptly dropped from 2016 to 2019 (Eayrs et al., 2021; Yang et al., 2021) with  
779 an all time-record low in 2023, driven by a complex and as yet poorly-understood combination of  
780 oceanic and atmospheric processes (Wang et al., 2024b). Climate model projections indicate major  
781 changes in the atmospheric circulation driven by the projected reduction in Antarctic sea ice in a  
782 warming climate: the Polar Cell and the katabatic flow off the coast of Antarctica are projected to  
783 strengthen, with a marginal weakening of the Ferrel and Hadley cells, and an equatorward shift in  
784 the position of the Polar Jet (Tewari et al., 2023). This stresses the need for a much-improved  
785 understanding of the observed variability of sea-ice properties, such as the SIE and SIT that are  
786 highly heterogeneous around Antarctica, to increase confidence in future climate-change  
787 projections. This is achieved in this study at a coastal site in East Antarctica through *in-situ*  
788 measurements for the period July–November 2022.

789

790 The SIT at the Khalifa SIMBA site on fast ice off Mawson Station largely follows the annual  
791 seasonal cycle, with a gradual increase during winter to mid-to-late October followed by a steady  
792 decline in late spring. The maximum values of  $\sim 1.1\text{--}1.2 \text{ m}$  are in the 0.50–1.50 m range estimated  
793 from satellite altimeter products for fast ice in the region around the Mawson Station (Li et al.,  
794 2022) and are also comparable to the thickness of pack ice around Antarctica (Kurtz and Markus,

795 2012; Kacimi and Kwok, 2020). The ST, on the other hand, is highly variable, with values in the  
796 range 0.02-0.18 m; these are also consistent with the estimates from satellite altimetry. In contrast  
797 to SIT, the temporal variability of ST is strongly linked to atmospheric forcing, in particular to  
798 precipitation (snowfall), Foehn effects, blowing snow, and episodic warm and moist air intrusions,  
799 which can lead to variations of up to  $\pm 0.08$  m in a day. During July-November 2022, an AR  
800 impacted the site on 14 July. It led to an 18 K increase in air temperature within 24 h, and a  
801 variation of up to 0.04 m in ST due to Foehn effects and snowfall (the 0.02 m change in SIT is  
802 within the estimated uncertainty range). These changes occurred within one day of the AR's  
803 arrival, followed by a recovery to pre-AR levels in the following 1-2 days. However, it is important  
804 to stress that a longer observational period would be needed to establish more robust and  
805 statistically significant links between atmospheric phenomena such as Foehn effects, blowing  
806 snow, and incursions of warm and moist low-latitude air and the coastal ST (and potentially SIT).  
807 In addition, having measurements for at least a full year would allow for the quantification of the  
808 potential role of surface melting in ST and SIT, which is more likely in the summer months but  
809 may occur at other times in a warming climate. Simulations with coupled ocean-atmosphere-sea-  
810 ice models should also be considered to further explore the role of atmospheric forcing in ST and  
811 SIT. In addition, refined methods to extract SIT and ST are desirable, as in particular for SIT, the  
812 variation during weather events such as the passage of the AR is within the uncertainty range,  
813 preventing a clear signal from being extracted from the data.

814  
815 The 14 July AR is particularly intense, with the highest IVT around the Khalifa SIMBA site  
816 on fast ice off Mawson Station of  $\sim 156 \text{ kg m}^{-1} \text{ s}^{-1}$ , which is in the top 0.5% of the climatological  
817 distribution. This AR has its origins in South America, where a wavetrain coming from the Pacific  
818 Ocean leads to an intensification of the South American Low-Level Jet and increased moisture  
819 outflow into the South Atlantic Ocean. The period 10-19 July 2022 is characterized by a  
820 wavenumber #5 pattern along the subtropical jet and a wavenumber #3 along the polar jet in the  
821 Southern Hemisphere, the latter projecting into the positive SAM phase, which is expected given  
822 the ongoing La Niña. A pressure dipole, with a low to the west and a ridge to the east, promotes  
823 the advection of warm and moist low-latitude air across Mawson Station. A back-trajectory  
824 analysis indicates contributions from evaporation both in the subtropics and the Southern Ocean  
825 to the precipitation event on 14 July 2022. A more in-depth analysis reveals that a secondary low  
826 formed just northwest of the site on 13 July, driven by high baroclinicity arising from the  
827 interaction of the warmer low-latitude air masses with the cold katabatic winds that prevail around  
828 Mawson Station. At the same time, a TPV and a jet streak at upper-levels contribute to an  
829 intensification of the primary low. The changing wind field in response to the passage of the deep  
830 cyclone, which had a central pressure as low as 931 hPa, also has an impact on the sea-ice  
831 dynamics. In particular, maximum pack-ice drift velocities north of Mawson Station exceeded 40  
832  $\text{km day}^{-1}$  from 12-14 July and 20  $\text{km day}^{-1}$  from 14-16 July with the opening of a polynya in the  
833 Southern Ocean northwest of Mawson Station around  $65^\circ\text{S}, 45^\circ\text{E}$  from 14 to 22 July. These pack-

834 ice drift speeds are comparable to those estimated during the opening of the Maud Rise Polynya  
835 in September 2017 (Francis et al., 2019).

836

837 A high-resolution simulation with PWRF down to 2.5 km is conducted to gain further insight  
838 into this event. An evaluation against *in-situ* observations indicates a good performance for both  
839 coastal and inland stations in the target region. A dry bias at coastal sites is attributed to an  
840 excessive offshore wind direction in the model and/or too much boundary layer mixing. An  
841 evaluation of the simulated vertical profiles against those observed at four coastal sites reveals a  
842 stronger katabatic flow in PWRF, which is consistent with the drier near-surface conditions.  
843 This is reported by other studies (e.g., Vignon et al., 2019), which attributed it to more stable  
844 boundary layers over the Antarctic Plateau and steeper land-sea synoptic pressure gradients. The  
845 overestimation of the surface upward longwave radiation flux may be a reflection of higher surface  
846 temperatures and/or a too high surface emissivity in PWRF. This suggests the need to optimize the  
847 land surface properties in the model, as has been highlighted by other studies (Hines et al., 2019).  
848 Ingesting a more realistic representation of the SIE and SIT does not translate into higher skill  
849 scores for this particular event. This indicates that improvements to the boundary layer dynamics  
850 and/or land/ice processes, noted by Wille et al. (2016, 2017) and Vignon et al. (2019), and at least  
851 for this case study, are probably more important than having a more accurate sea-ice representation  
852 in the model. Besides calibrating surface parameters, future PWRF studies should explore other  
853 physics schemes and/or optimize the tunable parameters defined inside the selected ones, in  
854 particular in the PBL and LSM as done for other regions (e.g., Quan et al., 2016; Chinta and Balaji,  
855 2020), in an attempt to improve the model performance. For example, the LSM employed, Noah-  
856 LSM, has a simplified representation of snow processes compared to the more sophisticated Noah-  
857 MP (Niu et al., 2011), which has shown higher skill over Antarctica (Xue et al., 2022). Adding a  
858 higher-resolution nest over the target region can also be beneficial as it will allow for a more  
859 accurate representation of dynamic and thermodynamic processes (Gilbert et al., 2025). The high-  
860 resolution PWRF simulation reveals the presence of AR rapids, with a similar vertical structure  
861 and propagation speed as those reported in Box et al. (2023) over Greenland in September 2017.  
862 The model simulation also highlights the effects of the katabatic wind regime in slowing down and  
863 weakening the low-latitude warm and moist air incursions as they approach the Antarctic coast. It  
864 is this interaction that triggers precipitation rates in excess of  $3 \text{ mm hr}^{-1}$  around Mawson Station  
865 during 14 July AR.

866

867 The SIMBA deployment at a fast ice site off Mawson Station during July-November 2022  
868 enabled a better understanding of the spatial and temporal variability of SIT and ST in that part of  
869 coastal East Antarctica. Such measurements should also be conducted at other sites given the  
870 marked regional differences in sea-ice properties in the Southern Ocean (Parkinson and Cavalieri,  
871 2012). This will also help to evaluate and improve the ST, SIE and SIT estimates derived from  
872 satellite remote sensing and numerical models. Besides ocean dynamics and thermodynamics, the  
873 findings of the study stress the role of atmospheric forcing in driving the variability in particular

874 of ST. Long-term measurements are needed to further explore and quantify how Foehn effects,  
875 blowing snow, warm and moist air intrusions, and surface melting modulate SIT and ST, and how  
876 they respond to seasonal and inter-annual variations in the atmospheric and oceanic state. This is  
877 a crucial step to improving the quality and confidence of future climate-change projections and  
878 medium- and long-range weather forecasts owing to the global influence of sea-ice variability on  
879 the climate system.

880

## 881 **Acknowledgements**

882 This work was funded by Khalifa University Polar Research Center. The authors wish to  
883 acknowledge the contribution of Khalifa University's high-performance computing and research  
884 computing facilities to the results of this research. The SIMBA deployment at a fast ice site the  
885 Mawson Station, *in-situ* measurements and the technical assistance were supported under  
886 Australian Antarctic Science [AAS] Project #4506 (CI: P. Heil). The work of P. Heil and R.  
887 Massom was supported by the Australian Antarctic Division. For R. Massom, this work was also  
888 supported by the Australian Research Council Special Research Initiative the Australian Centre  
889 for Excellence in Antarctic Science (Project Number SR200100008). PH acknowledges support  
890 from the AAS Program (AAS4496, AAS4506, AAS4625) and grant funding from the International  
891 Space Science Institute (Switzerland; Project 405) and the Swiss Federal Research Fellowship  
892 program. For P. Heil and R. Massom, this work contributes to Project 6 of the Australian Antarctic  
893 Program Partnership (ASCI00002) funded under the Australian Government's Antarctic Science  
894 Collaboration Initiative program. We are also grateful for the Byrd Polar and Climate Research  
895 Center at The Ohio State University for developing and maintaining PolarWRF and making it  
896 freely available to the scientific community. We greatly appreciate the support of the Automatic  
897 Weather Station Program and the Antarctic Meteorological Research Center for the weather station  
898 data used in this study (National Science Foundation grants numbers ARC-0713843, ANT-  
899 0944018, and ANT-1141908). The authors also gratefully acknowledge the National Oceanic and  
900 Atmospheric Administration Air Resources Laboratory for the provision of the Hybrid Single-  
901 Particle Lagrangian Integrated Trajectory (HYSPLIT) transport and dispersion model used in this  
902 work. We would like to thank the editor and two anonymous reviewers for their insightful and  
903 constructive comments and suggestions that helped to substantially improve the quality of this  
904 work.

905

## 906 **Code/Data availability**

907 The sea-ice and snow thickness measurements at the Khalifa SIMBA site on fast ice off Mawson  
908 Station for July-November 2022 are available upon request from the corresponding author (Diana  
909 Francis; [diana.francis@ku.ac.ae](mailto:diana.francis@ku.ac.ae)). The remaining observational and the reanalysis datasets used in

910 this study are freely available online: (i) ERA-5 reanalysis data were downloaded from the  
911 Copernicus Climate Data Store website (Hersbach et al., 2023a,b); (ii) Automatic Weather Station  
912 (AWS) data at the Mawson, Davis, and Casey Stations can be requested at the Australian Antarctic  
913 Data Center website (AADC, 2022); (iii) AWS and surface radiation data for Syowa Station were  
914 obtained from the World Radiation Monitoring Center - Baseline Surface Radiation Network  
915 website (AWI, 2024); (iv) AWS data for the Relay Station was extracted from the Antarctic  
916 Meteorological Research Center & Automatic Weather Stations Project (Lazzara, 2024); (v) sea-  
917 ice velocity vectors from the low resolution sea-ice drift product are available at the European  
918 Organization for the Exploitation of Meteorological Satellites (EUMETSAT) Ocean and Sea Ice  
919 Satellite Application Facility (EUMETSAT, 2024); (vi) sea-ice concentration maps derived from  
920 the measurements collected by the Advanced Microwave Scanning Radiometer (AMSR) for Earth  
921 Observing Systems instrument onboard the National Aeronautics and Space Administrations  
922 (NASA) Aqua satellite and the AMSR-2 instrument onboard the Japan Aerospace and Exploration  
923 Agency Global Change Observation Mission 1<sup>st</sup>-Water “Shizuku” satellite from January 2013 to  
924 present, were obtained from the University of Bremen website (UoB; 2024); (vii) twice daily  
925 atmospheric sounding profiles at the Mawson, Syowa, Davis, and Casey stations were accessed at  
926 the University of Wyoming website (Oolman, 2025). The Hybrid Single-Particle Lagrangian  
927 Integrated Trajectory (HYSPLIT) transport and dispersion model is downloaded from the National  
928 Aeronautic and Space Administration Air Resources Laboratory website (NOAA ARL, 2024). The  
929 PolarWRF model version 4.3.3 is available at the Byrd Polar and Climate Research Center at The  
930 Ohio State University website (PWRF, 2024). The figures presented in this manuscript have been  
931 generated with the Interactive Data Language (IDL; Bowman, 2005) and MATLAB (Mathworks,  
932 2024) software.

933

### 934 Competing interests

935

936 One co-author is a member of The Cryosphere editorial board.

937

### 938 Author Contributions: CRediT

939 **DF**: Conceptualization of the study, Interpretation and validation of the results, Writing the draft,  
940 Funding Acquisition; **RF**: Formal analysis, Data processing and analysis of the results, Writing  
941 the draft; **NN**: Data acquisition, processing and analysis, Interpretation of the results, Inputs to the  
942 manuscript; **PH**: Interpretation of the results, Inputs to the manuscript; **JDW**: Interpretation of the  
943 results, Inputs to the manuscript; **IVG**: Interpretation of the results, Inputs to the manuscript;  
944 **RAM**: Interpretation of the results, Inputs to the manuscript. All authors interpreted the results and  
945 provided input to the final manuscript.

946 **References**

947 AADC (2022) Antarctic Climate Data Collected by Australian Agencies. Australian Antarctic Data Center  
948 [Dataset]. Accessed on 22 April 2024, available online at [Australian Antarctic Data Centre \(aad.gov.au\)](https://www.aad.gov.au).

949

950 Alapaty, K., Herwehe, J. A., Otte, T. L., Nolte, C. G., Bullock, O. R., Mallard, M. S., Kain, J. S., Dudhia,  
951 J. (2012) Introducing subgrid-scale cloud feedbacks to radiation for regional meteorological and climate  
952 modeling. *Geophysical Research Letters*, 39, L24809. <https://doi.org/10.1029/2012GL054031>

953

954 Attada, R., Kunchala, R. K., Dasari, H. P., Sivareddy, S., Yesubabu, V., Knio, O., Hoteit, I. (2021)  
955 Representation of Arabian Peninsula summer climate in a regional atmospheric model using spectral  
956 nudging. *Theoretical and Applied Climatology*, 145, 13-30. <https://doi.org/10.1007/s00704-021-03617-w>

957

958 AWI (2024). WRMC-BSRN: World Radiation Monitoring Center - Baseline Surface Radiation Network  
959 [Dataset]. Accessed on 15 April 2024, available online at <https://bsrn.awi.de/>.

960

961 Barber, D. G., Massom, R. A. (2007) The Role of Sea Ice in Arctic and Antarctic Polynyas. In W. O. Smith  
962 and D. G. Barber (Editors), *Polynyas: Windows to the World's Oceans*, pp. 1-54. Elsevier. Amsterdam.

963

964 Bowman, K. P. (2005) An Introduction to Programming with IDL: Interactive Data Language [Software].  
965 Academic Press, 304 pp.. ISBN-10: 012088559X, ISBN-13: 978-0120885596.

966

967 Box, J. E., Nielsen, K. P., Yang, X., Niwano, M., Wehrle, A., van As, D., Fettweis, X., Koltzow, M. A. O.,  
968 Palmason, B., Fausto, R. S., van den Broeke, M. R., Huai, B., Ahlstrom, A. P., Langley, K., Dachauer, A.,  
969 Noel, B. (2023) Greenland ice sheet rainfall climatology, extremes and atmospheric river rapids.  
970 *Meteorological Applications*, 30, e2134. <https://doi.org/10.1002/met.2134>

971

972 Bozkurt, D., Rondanelli, R., Marin, J. C., Garreaud, R. (2018) Foehn event triggered by an atmospheric  
973 river underlies record-setting temperature along continental Antarctica. *Journal of Geophysical Research: Atmospheres*, 123, 3871-3892. <https://doi.org/10.1002/2017JD027796>

974

975

976 Bromwich, D. H., Otieno, F. O., Hines, K. M., Manning, K. W., Shilo, E. (2013) Comprehensive evaluation  
977 of polar weather research and forecasting model performance in the Antarctic. *Journal of Geophysical  
978 Research: Atmospheres*, 118, 274-292. <https://doi.org/10.1029/2012JD018139>

979

980 Bromwich, D. H., Powers, J. G., Manning, K. W., Zou, X. (2022) Antarctic data impact experiments with  
981 Polar WRF during the YOPP-SH summer special observing period. *Quarterly Journal of the Royal  
982 Meteorological Society*, 148, 2194-2218. <https://doi.org/10.1002/qj.4298>

983

984 Chen, F., Dudhia, J. (2001) Coupling an Advanced Land Surface-Hydrology Model with the Penn State -  
985 NCAR MM5 Modeling System. Part I: Model Implementation and Sensitivity. *Monthly Weather Review*,  
986 129, 569-585. [https://doi.org/10.1175/1520-0493\(2001\)129<0569:CAALSH>2.0.CO;2](https://doi.org/10.1175/1520-0493(2001)129<0569:CAALSH>2.0.CO;2)

987

988 Chinta, S., Balaji, C. (2020) Calibration of WRF model parameters using multiobjective adaptive surrogate  
989 model-based optimization to improve the prediction of the Indian summer monsoon. *Climate Dynamics*,  
990 55, 631-650. <https://doi.org/10.1007/s00382-020-05288-1>

991

992 Dare, R. A., Budd, W. F. (2001) Analysis of Surface Winds at Mawson, Antarctica. *Weather and*  
993 *Forecasting*, 16, 416-431. [https://doi.org/10.1175/1520-0434\(2001\)016<0416:AOSWAM>2.0.CO;2](https://doi.org/10.1175/1520-0434(2001)016<0416:AOSWAM>2.0.CO;2)

994

995 Djoumna, G., Holland, D. M. (2021) Atmospheric rivers, warm air intrusions, and surface radiation balance  
996 in the Amundsen Sea Embayment. *Journal of Geophysical Research: Atmospheres*, 126, e2020JD034119.  
997 <https://doi.org/10.1029/2020JD034119>

998

999 Dery, S. J., Yau, M. K. (2002) Large-scale mass balance effects of blowing snow and surface sublimation.  
1000 *Journal of Geophysical Research*, 107, 4679. <https://doi.org/10.1029/2001JD001251>

1001

1002 Dong, X., Wang, Y., Hou, S., Ding, M., Yin, B., Zhang, Y. (2020) Robustness of the Recent Global  
1003 Atmospheric Reanalyses for Antarctic Near-Surface Wind Speed Climatology. *Journal of Climate*, 33,  
1004 4027-4043. <https://doi.org/10.1175/JCLI-D-19-0648.1>

1005

1006 Eayrs, C., Holland, D. M., Francis, D., Wagner, T. J. W., Kumar, R., Li, X. (2019) Understanding the  
1007 seasonal cycle of Antarctic sea ice extent in the context of long-term variability. *Reviews of Geophysics*,  
1008 57, 1037-1064. <https://doi.org/10.1029/2018RG000631>

1009

1010 Eayrs, C., Li, X., Raphael, M. N., Holland, D. M. (2021) Rapid decline in Antarctic sea ice in recent years  
1011 hints at future change. *Nature Geosciences*, 14, 460-464. <https://doi.org/10.1038/s41561-021-00768-3>

1012

1013 Elvidge, A. D., Munneke, K., King, P., Renfrew, I. A., Gilbert, E. (2020) Atmospheric drivers of melt on  
1014 Larsen C Ice Shelf: Surface energy budget regimes and the impact of foehn. *Journal of Geophysical*  
1015 *Research: Atmospheres*, 125, e2020JD032463. <https://doi.org/10.1029/2020JD032463>

1016

1017 England, M. R., Wagner, T. J. W., Eisenman, I. (2020) Modeling the breakup of tabular icebergs. *Science*  
1018 *Advances*, 6, 51. <https://doi.org/10.1126/sciadv.abd1273>

1019

1020 EUMETSAT (2024) Ocean and Sea Ice Satellite Application Facility. Accessed on 12 August 2024,  
1021 available online at <https://osi-saf.eumetsat.int/products/osi-405-c>

1022

1023 Feng, Z., Leung, L. R., Liu, N., Wang, J., Houze, R. A. Jr., Li, J., Hardin, J. C., Chen, D., Guo, J. (2021) A  
1024 global high-resolution mesoscale convective system database using satellite-derived cloud tops, surface  
1025 precipitation, and tracking. *Journal of Geophysical Research: Atmospheres*, 126, e2020JD034202.  
1026 <https://doi.org/10.1029/2020JD034202>

1027

1028 Finlon, J. A., Rauber, R. M., Wu, W., Zaremba, T. J., McFarquhar, G. M., Nesbitt, S. W., Schnaiter, M.,  
1029 Jarvinen, E., Waitz, F., Hill, T. C. J., DeMott, P. J. (2020) Structure of an atmospheric river over Australia  
1030 and the Southern Ocean: II. Microphysical evolution. *Journal of Geophysical Research: Atmospheres*, 125,  
1031 e2020JD032514. <https://doi.org/10.1029/2020JD032514>

1032  
1033 Fogt, R. L., Bromwich, D. H., Hines, K. M. (2011) Understanding the SAM influence on the South Pacific  
1034 ENSO teleconnection. *Climate Dynamics*, 36, 1555-1576. <https://doi.org/10.1007/s00382-010-0905-0>  
1035  
1036 Fons, S., Kurtz, N., Bagnardi, M. (2023) A decade-plus of Antarctic sea ice thickness and volume estimates  
1037 from CryoSat-2 using a physical model and waveform fitting. *The Cryosphere*, 17, 2487-2508.  
1038 <https://doi.org/10.5194/tc-17-2487-2023>  
1039  
1040 Fonseca, R., Francis, D., Aulicino, G., Mattingly, K., Fusco, G., Budillon, G. (2023) Atmospheric controls  
1041 on the Terra Nova Bay polynya occurrence in Antarctica. *Climate Dynamics*, 61, 5147-5169.  
1042 <https://doi.org/10.1007/s00382-023-06845-0>  
1043  
1044 Francis, D., Eayrs, C., Cuesta, J., Holland, D. (2019) Polar cyclones at the origin of the reoccurrence of the  
1045 Maud Rise Polynya in austral winter 2017. *Journal of Geophysical Research: Atmospheres*, 124, 5251-  
1046 5267. <https://doi.org/10.1029/2019JD030618>  
1047  
1048 Francis, D., Fonseca, R., Bozkurt, D., Nelli, N., Guan, B. (2024) Atmospheric River Rapids and Their Role  
1049 in the Extreme Rainfall Event of April 2023 in the Middle East. *Geophysical Research Letters*, 51,  
1050 e2024GL109446. <https://doi.org/10.1029/2024GL109446>  
1051  
1052 Francis, F., Fonseca, R., Mattingly, K. S., Lhermitte, S., Walker, C. (2023) Foehn winds at Pine Island  
1053 Glacier and their role in ice changes. *The Cryosphere*, 17, 3041-3062. <https://doi.org/10.5194/tc-17-3041-2023>  
1055  
1056 Francis, D., Fonseca, R., Nelli, N., Bozkurt, D., Picard, G., Guan, B. (2022a) Atmospheric rivers drive  
1057 exceptional Saharan dust transport towards Europe. *Atmospheric Research*, 266, 105959.  
1058 <https://doi.org/10.1016/j.atmosres.2021.105959>  
1059  
1060 Francis, D., Mattingly, K. S., Lhermitte, S., Temimi, M., Heil, P. (2021) Atmospheric extremes caused high  
1061 oceanward sea surface slope triggering the biggest calving event in more than 50 years at the Amery Ice  
1062 Shelf. *The Cryosphere*, 15, 2147-2165. <https://doi.org/10.5194/tc-15-2147-2021>  
1063  
1064 Francis, D., Fonseca, R., Mattingly, K. S., Marsh, O. J., Lhermitte, S., Cherif, C. (2022b) Atmospheric  
1065 triggers of the Brunt Ice Shelf calving in February 2021. *Journal of Geophysical Research: Atmospheres*,  
1066 127, e2021JD036424. <https://doi.org/10.1029/2021JD036424>  
1067  
1068 Francis, D., Mattingly, K. S., Temimi, M., Massom, R., Heil, P. (2020) On the crucial role of atmospheric  
1069 rivers in the two major Weddell Polynya events in 1973 and 2017 in Antarctica. *Science Advances*, 6.  
1070 <https://doi.org/10.1126/sciadv.abc2695>  
1071  
1072 Fraser, A. D., Wongpan, P., Langhorne, P. J., Klekociuk, A. R., Kusahara, K., Lannuzel, D., Massom, R.  
1073 A., Meiners, K. M., Swadling, K. M., Atwater, D. P., Brett, G. M., Corkill, M., Dalman, L. A., Fiddes, S.,  
1074 Granata, A., Guglielmo, L., Heil, P., Leonard, G. H., Mahoney, A. R., McMinn, A., van der Merwe, P.,

1075 Weldrick, C. K., Wienecke, B. (2023) Antarctic landfast sea ice: A review of its physics, biogeochemistry  
1076 and ecology. *Reviews of Geophysics*, 61, e2022RG000770. <https://doi.org/10.1029/2022RG000770>

1077

1078 Gehring, J., Vignon, E., Billault-Roux, A. C., Ferrone, A., Protat, A., Alexander, S. P., Berne, A. (2022)  
1079 Orographic flow influence on precipitation during an atmospheric river event at Davis, Antarctica. *Journal*  
1080 *of Geophysical Research: Atmospheres*, 127, e2021JD035210. <https://doi.org/10.1029/2021JD035210>.

1081

1082 Ghiz, M.L., Scott, R. C., Vogelmann, A. M., Lenaerts, J. T. M., Lazzara, M., Lubin, D. (2021) Energetics  
1083 of surface melt in West Antarctica. *The Cryosphere*, 15, 3459-3494. <https://doi.org/10.5194/tc-15-3459-2021>

1085

1086 Gilbert, E., Pishniak, D., Torres, J. A., Orr, A., Maclennan, M., Wever, N., Verro, K. (2025) Extreme  
1087 precipitation associated with atmospheric rivers over West Antarctic ice shelves: insights from the  
1088 kilometre-scale regional climate modeling. *The Cryosphere*, 19, 597-618. <https://doi.org/10.5194/tc-19-597-2025>

1090

1091 Goosse, H., Contador, A., Bitz, C., Blanchard-Wrigglesworth, C. M., Eayrs, E., Fichefet, C., Himmich, T.,  
1092 Huot, K., Klein, P.-V., Marchi, F., Massonnet, S., Mezzina, F., Pelletier, B., Roach, C., Vancoppenolle, L.,  
1093 van Lipzig, N. P. M. (2023) Modulation of the seasonal cycle of the Antarctic sea ice extent by sea ice  
1094 processes and feedbacks with the ocean and the atmosphere. *The Cryosphere*, 17, 407-425.  
1095 <https://doi.org/10.5194/tc-17-407-2023>

1096

1097 Gorodetskaya, I. V., Duran-Alarcon, C., Gonzalez-Herrero, S., Clem, K. R., Zou, X., Rowe, P., Imazio, P.  
1098 R., Campos, D., Leroy-Dos Santos, C., Dutrievoz, N., Wille, J. D., Chyhareva, A., Favier, V., Blanchet, J.,  
1099 Pohl, B., Cordero, R. R., Prak, S.-J., Colwell, S., Lazzara, M. A., Carrasco, J., Gulisano, A. M., Krakovska,  
1100 S., Ralph, F. M., Dethinne, T., Picard, G. (2023) Record-high Antarctic Peninsula temperatures and surface  
1101 melt in February 2022: a compound event with an intense atmospheric river. *Npj Climate and Atmospheric*  
1102 *Science*, 6, 202. <https://doi.org/10.1038/s41612-023-00529-6>

1103

1104 Gorodetskaya, I. V., Silva, T., Schmithusen, H., Hirasawa, N. (2020) Atmospheric river signatures in  
1105 radiosonde profiles and reanalyses at the Dronning Maud Land Coast, East Antarctica. *Advances in*  
1106 *Atmospheric Sciences*, 37, 455-476. <https://doi.org/10.1007/s00376-020-9221-8>

1107

1108 Gorodetskaya, I. V., Van Lipzig, N. P. M., Van den Broeke, M. R., Mangold, A., Boot, W., Reijmer, C. H.  
1109 (2013) Meteorological regimes and accumulation patterns at Utsteinen, Dronning Maud Land, East  
1110 Antarctica: Analysis of two contrasting years. *Journal of Geophysical Research: Atmospheres*, 118, 1700-  
1111 1715. <https://doi.org/10.1002/jgrd.50177>

1112

1113 Gossart, A., Helsen, S., Lenaerts, J. T. M., Vanden Broucke, S., van Lipzig, N. P. M., Souverijns, N. (2019)  
1114 An Evaluation of Surface Climatology in State-of-the-Art Reanalyses over the Antarctic Ice Sheet. *Journal*  
1115 *of Climate*, 32, 6899-6915. <https://doi.org/10.1175/JCLI-D-19-0030.1>

1116

1117 Guest, P. S. (2021) Inside katabatic winds over the Terra Nova Bay polynya: 2. Dynamic and  
1118 thermodynamic analyses. *Journal of Geophysical Research: Atmospheres*, 126, e2021JD034904.  
1119 <https://doi.org/10.1029/2021JD034904>

1120

1121 Haas, C. (2017) Sea ice thickness distribution. In: *Sea Ice*, D. N. Thomas (Ed.). Blackwell Science.  
1122 <https://doi.org/10.1002/9781118778371.ch2>

1123

1124 Haumann, F. A., Gruber, N., Munnich, M., Frenger, I., Kern, S. (2016) Sea-ice transport driving Southern  
1125 Ocean salinity and its recent trends. *Nature*, 537, 89-92. <https://doi.org/10.1038/nature19101>

1126

1127 Heil, P. (2006) Atmospheric conditions and fast ice at Davis, East Antarctica: A case study. *Journal of  
1128 Geophysical Research*, 111, C05009. <https://doi.org/10.1029/2005JC002904>

1129

1130 Heil, P., Allison, I., Lytle, V. I. (1996) Seasonal and interannual variations of the oceanic heat flux under a  
1131 landfast Antarctic sea ice cover. *Journal of Geophysical Research*, 101(C11), 25741-25752.  
1132 <https://doi.org/10.1029/96JC01921>

1133

1134 Hersbach, H., Bell, B., Berrisford, P., Biavati, G., Horanyi, A., Munoz Sabater, J., Nicolas, J., Peavey, C.,  
1135 Radu, R., Rozum, I., Schepers, D., Simmons, A., Soci, C., Dee, D., Thepaut, J.-N. (2023a) ERA5 hourly  
1136 data on single levels from 1940 to present [Dataset]. Copernicus Climate Change Service (C3S) Climate  
1137 Data Store (CDS). Accessed on 22 April 2024, available online at <https://doi.org/10.24381/cds.adbb2d47>

1138

1139 Hersbach, H., Bell, B., Berrisford, P., Biavati, G., Horanyi, A., Munoz Sabater, J., Nicolas, J., Peavey, C.,  
1140 Radu, R., Rozum, I., Schepers, D., Simmons, A., Soci, C., Dee, D., Thepaut, J.-N. (2023b) ERA5 hourly  
1141 data on pressure levels from 1940 to present [Dataset]. Copernicus Climate Change Service (C3S) Climate  
1142 Data Store (CDS). Accessed on 22 April 2024, available online at <https://doi.org/10.24381/cds.bd0915c6>

1143

1144 Hersbach, H., Bell, B., Berrisford, P., Hirahara, S., Horanyi, A., Munoz-Sabater, J., Nicolas, J., Peavey, C.,  
1145 Radu, R., Schepers, D., Simmons, A., Soci, C., Abdalla, S., Abellana, X., Balsamo, G., Bechtold, P., Biavati,  
1146 G., Bidiot, J., Bonavita, M., De Chiara, G., Dahlgren, P., Dee, D., Diamantakis, M., Dragani, R., Fleming,  
1147 J., Forbes, R., Fuentes, M., Geer, A., Haimberger, L., Healy, S., Hogan, R. J., Holm, E., Janiskova, M.,  
1148 Keeley, S., Laloyaux, P., Lopez, P., Lulu, C., Radnoti, G., de Rosnay, P., Rozum, I., Vamborg, F., Villaume,  
1149 S., Thepaut, J.-N. (2020) The ERA5 global reanalysis. *Quarterly Journal of the Royal Meteorological  
1150 Society*, 146, 1999-2049. <https://doi.org/10.1002/qj.3803>

1151

1152 Hines, K. M., Bromwich, D. H., Silber, I., Russell, L. M., Bai, L. (2021) Predicting frigid mixed-phase  
1153 clouds for pristine coastal Antarctica. *Journal of Geophysical Research: Atmospheres*, 126,  
1154 e2021JD035112. <https://doi.org/10.1029/2021JD035112>

1155

1156 Hines, K. M., Bromwich, D. H., Wang, S.-H., Silber, I., Verlinde, J., Lubin, D. (2019) Microphysics of  
1157 summer clouds in central West Antarctica simulated by the Polar Weather Research and Forecasting Model  
1158 (WRF) an the Antarctic Mesoscale Prediction System (AMPS). *Atmospheric Chemistry and Physics*, 19,  
1159 12431-12454. <https://doi.org/10.5194/acp-19-12431-2019>

1160

1161 Hobbs, W., Spence, P., Meyer, A., Schroeter, S., Fraser, A. D., Reid, P., Tian, R. T., Wang, Z., Liniger, G.,  
1162 Doddridge, E. W., Boyd, P. W. (2024) Observational Evidence for a Regime Shift in Summer Antarctic  
1163 Sea Ice. *Journal of Climate*, 37, 2263-2275. <https://doi.org/10.1175/JCLI-D-23-0479.1>

1164

1165 Hoppmann, M., M. Nicolaus, P. A. Hunkeler, P. Heil, L.-K. Behrens, G. König-Langlo, R. Gerdes (2015)  
1166 Seasonal evolution of an ice-shelf influenced fast-ice regime, derived from an autonomous thermistor chain.  
1167 *Journal of Geophysical Research: Oceans*, 120, 1703–1724, <https://doi.org/10.1002/2014JC010327>.

1168

1169 Hoskins, B., Fonseca, R., Blackburn, M., Jung, T. (2012) Relaxing the Tropics to an ‘observed’ state:  
1170 analysis using a simple baroclinic model. *Quarterly Journal of the Royal Meteorological Society*, 138, 1618–  
1171 1626. <https://doi.org/10.1002/qj.1881>

1172

1173 Hoskins, B. J., Karoly, D. J. (1981) The Steady Linear Response of a Spherical Atmosphere to Thermal  
1174 and Orographic Forcing. *Journal of Atmospheric Sciences*, 38, 1179-1196. [https://doi.org/10.1175/1520-0469\(1981\)038<1179:TSLROA>2.0.CO;2](https://doi.org/10.1175/1520-0469(1981)038<1179:TSLROA>2.0.CO;2)

1176

1177 Hoskins, B. J., Valdes, P. J. (1990) On the Existence of Storm-Tracks. *Journal of Atmospheric Sciences*,  
1178 47, 1854-1864. [https://doi.org/10.1175/1520-0469\(1990\)047<1854:OTEOST>2.0.CO;2](https://doi.org/10.1175/1520-0469(1990)047<1854:OTEOST>2.0.CO;2)

1179

1180 Houze, R. A. Jr. (2004) Mesoscale convective systems. *Reviews of Geophysics*, 42, RG4003.  
1181 <https://doi.org/10.1029/2004RG000150>

1182

1183 Hu, H., Zhao, J., Heil, P., Qin, Z., Ma, J., Hui, F., Cheng, X. (2023) Annual evolution of the ice-ocean  
1184 interaction beneath landfast ice in Prydz Bay, East Antarctica. *The Cryosphere*, 17, 2231-2244.  
1185 <https://doi.org/10.5194/tc-17-2231-2023>

1186

1187 Iacono, M. J., Delamere, J. S., Mlawer, E. J., Shephard, M. W., Clough, S. A., & Collins, W. D. (2008)  
1188 Radiative forcing by long-lived greenhouse gasses: Calculations with the AER radiative transfer models.  
1189 *Journal of Geophysical Research*, 113, D13103. <https://doi.org/10.1029/2008JD009944>

1190

1191 Jackson, K., J. Wilkinson, T. Maksym, D. Meldrum, J. Beckers, C. Haas, and D. Mackenzie (2013) A Novel  
1192 and Low Cost Sea Ice Mass Balance Buoy. *Journal of Atmospheric and Oceanic Technology*, 30, 2676–  
1193 2688. <https://doi.org/10.1175/JTECH-D-13-00058.1>

1194

1195 Kacimi, S., Kwok, R. (2020) The Antarctic sea ice cover from ICESat-2 and CryoSat-2: freeboard, snow  
1196 depth, and ice thickness. *The Cryosphere*, 14, 4453-4474. <https://doi.org/10.5194/tc-14-4453-2020>

1197

1198 Kain, J. S. (2004) The Kain-Fritsch convective parameterization: An update. *Journal of Applied  
1199 Meteorology*, 43, 170-181. [https://doi.org/10.1175/1520-0430\(2004\)043<0170:tkcpau>2.0.co;2](https://doi.org/10.1175/1520-0430(2004)043<0170:tkcpau>2.0.co;2)

1200

1201 Kawamura, T., Takizawa, T., Ohshima, K. I., Ushio, S. (1995) Data of sea-ice cores obtained in Lutzow-  
1202 Holm Bay from 1990 to 1992 (JARE-31, -32) in the period of Japanese Antarctic climate research. *JARE  
1203 Data Rep.* 204 (Glaciol. 24), 42 pp., National Institute of Polar Research, Tokyo.

1204

1205 Koh, T.-Y., Wang, S., Bhatt, B. C. (2012) A diagnostic suite to assess NWP performance. *Journal of*  
1206 *Geophysical Research*, 117, D13109. <https://doi.org/10.1029/2011JD017103>

1207

1208 Kuipers Munneke, P., McGrath, D., Medley, B., Luckman, A., Bevan, S., Kulessa, B., Jansen, D., Booth,  
1209 A., Smeets, P., Hubbard, B., Ashmore, D., Van den Broeke, M., Sevestre, H., Steffen, K., Shepherd, A.,  
1210 Gourmelen, N. (2017) Observationally constrained surface mass balance of Larsen C ice shelf, Antarctica.  
1211 *The Cryosphere*, 11, 2411-2426. <https://doi.org/10.5194/tc-11-2411-2017>

1212

1213 Kurtz, N. T., Markus, T. (2012) Satellite observations of Antarctic sea ice thickness and volume. *Journal*  
1214 *of Geophysical Research*, 117, C08025. <https://doi.org/10.1029/2012JC008141>

1215

1216 Lavergne, T., Eastwood, S., Teffah, Z., Schuberg, H., Breivik, L.-A. (2010) Sea ice motion from low-  
1217 resolution satellite sensors: an alternative method and its validation in the Arctic. *Journal of Geophysical*  
1218 *Research: Oceans*, 115, C10032. <https://doi.org/10.1029/2009JC005958>

1219

1220 Laffin, M. K., Zender, C. S., Singh, S., Van Wessem, J. M., Smeets, C. J. P. P., Reijmer, C. H. (2021)  
1221 Climatology and evolution of the Antarctic Peninsula fohn wind-induced melt regime from 1979-2018.  
1222 *Journal of Geophysical Research: Atmospheres*, 126, e2020JD033682.  
1223 <https://doi.org/10.1029/2020JD033682>

1224

1225 Lazzara, M. (2024) Antarctic Meteorological Research Center & Automatic Weather Stations Project  
1226 [Dataset]. Accessed on 12 May 2024, available online at <https://amrc.ssec.wisc.edu/>.

1227

1228 Lea, E. J., Jamieson, S. S. R., Bentley, M. J. (2024) Alpine topography of the Gamburtsev Subglacial  
1229 Mountains, Antarctica, mapped from ice sheet surface morphology. *The Cryosphere*, 18, 1733-1751.  
1230 <https://doi.org/10.5194/tc-18-1733-2024>

1231

1232 Li, H., Fedorov, A. V. (2021) Persistent freshening of the Arctic Ocean and changes in the North Atlantic  
1233 salinity caused by Arctic sea ice decline. *Climate Dynamics*, 57, 2995-3013.  
1234 <https://doi.org/10.1007/s00382-021-05850-5>

1235

1236 Li, X.-Q., Hui, F.-M., Zhao, J.-C., Zhai, M.-X., Cheng, X. (2022) Thickness simulation of landfast ice  
1237 along Mawson Coast, East Antarctica based on a snow/ice high-resolution thermodynamic model.  
1238 *Advances in Climate Change Research*, 13, 375-384. <https://doi.org/10.1016/j.accre.2022.05.005>

1239

1240 Liang, K., Wang, J., Luo, H., Yang, Q. (2023) The role of atmospheric rivers in Antarctic sea ice variations.  
1241 *Geophysical Research Letters*, 50, e2022GL102588. <https://doi.org/10.1029/2022GL102588>

1242

1243 Liao, Z., Cheng, B., Zhao, J., Vihma, T., Jackson, K., Yang, Q., Yang, Y., Zhang, L., Li, Z., Qiu, Y., Cheng,  
1244 X. (2018). Snow depth and ice thickness derived from SIMBA ice mass balance buoy data using an  
1245 automated algorithm. *International Journal of Digital Earth*, 12(8), 962-979.  
1246 <https://doi.org/10.1080/17538947.2018.1545877>

1247

1248 Liao, S., Luo, H., Wang, J., Shi, Q., Zhang, J., Yang, Q. (2022) An evaluation of Antarctic sea-ice thickness  
1249 from the Global Ice-Ocean Modeling and Assimilation System based on it situ and satellite observations.  
1250 The Cryosphere, 16, 1807-1819. <https://doi.org/10.5194/tc-16-1807-2022>

1251

1252 Lim, S., Gim, H.-J., Lee, E., Lee, S., Lee, W. Y., Lee, Y. H., Cassardo, C., Park, S. K. (2022) Optimization  
1253 of snow-related parameters in the Noah land surface model (v3.4.1) using a micro-genetic algorithm  
1254 (v1.7a). Geoscientific Model Development, 15, 8541-8559. <https://doi.org/10.5194/gmd-15-8541-2022>

1255

1256 Maksym, T., Markus, T. (2008) Antarctic sea ice thickness and snow-to-ice conversion from atmospheric  
1257 reanalysis and passive microwave snow depth. Journal of Geophysical Research, 113, C02S12.  
1258 <https://doi.org/10.1029/2006JC004085>

1259

1260 Maksym, T., Stammerjohn, S., Ackley, S., Massom, R. (2012) Antarctic sea ice – A polar opposite?  
1261 Oceanography 25, 140-151. <https://doi.org/10.5670/oceanog.2012.88>

1262

1263 Marengo, J. A., Soares, W. R., Saulo, C., Nicolini, M. (2004) Climatology of the Low-Level Jet East of the  
1264 Andes as Derived from the NCEP-NCAR Reanalyses: Characteristics and Temporal Variability. Journal of  
1265 Climate, 17, 2261-2280. [https://doi.org/10.1175/1520-0442\(2004\)017<2261:COTLJE>2.0.CO;2](https://doi.org/10.1175/1520-0442(2004)017<2261:COTLJE>2.0.CO;2)

1266

1267 Marshall, G. J. (2003) Trends in the Southern Annular Mode from Observations and Reanalyses. Journal  
1268 of Climate, 16, 4134-4143. [https://doi.org/10.1175/1520-0442\(2003\)016<4134:TITSAM>2.0.CO;2](https://doi.org/10.1175/1520-0442(2003)016<4134:TITSAM>2.0.CO;2)

1269

1270 Massom, R.A., H. Eicken, C. Haas, M.O. Jeffries, M.R. Drinkwater, M. Sturm, A.P. Worby, X. Wu, V.I.  
1271 Lytle, S. Ushio, K. Morris, P.A. Reid, S. Warren, and I. Allison. (2001) Snow on Antarctic sea ice. Reviews  
1272 of Geophysics, 39(3), 413-445. <https://doi.org/10.1029/2000RG000085>

1273

1274 Massom, R. A., Pook, M. J., Comiso, J. C., Adams, N., Turner, J., Lachlan-Cope, T., Gibson, T. T. (2004)  
1275 Precipitation over the interior East Antarctic Ice Sheet related to mid-latitude blocking-high activity.  
1276 Journal of Climate, 17, 1914-1928. [https://doi.org/10.1175/1520-0442\(2004\)017%3C1914:POTIEA%3E2.0.CO;2](https://doi.org/10.1175/1520-0442(2004)017%3C1914:POTIEA%3E2.0.CO;2)

1277

1278

1279 Massonnet, F., Mathiot, P., Fichefet, T., Goosse, H., Beatty, C. K., Vancopenolle, M., Lavergne, T. (2013)  
1280 A model reconstruction of the Antarctic sea ice thickness and volume changes over 1980-2008 using data  
1281 assimilation. Ocean Modeling, 64, 67-75. <https://doi.org/10.1016/j.ocemod.2013.01.003>

1282

1283 Matejka, M., Laska, K., Jeklova, K., Hosek, J. (2021) High-Resolution Numerical Modeling of Near-  
1284 Surface Atmospheric Fields in the Complex Terrain of James Ross Island, Antarctic Peninsula.  
1285 Atmosphere, 12, 360. <https://doi.org/10.3390/atmos12030360>

1286

1287 Mathworks (2024) Math. Graphics. Programming [Software]. Accessed on 18 March 2024, available online  
1288 at <https://uk.mathworks.com/products/matlab.html>

1289

1290 McLennan, M. L., Lenaerts, J. T. M., Shields, C. A., Hoffman, A. O., Wever, N., Thompson-Munson, M.,  
1291 Winters, A. C., Pettit, E. C., Scambos, T. A., Wille, J. D. (2023) Climatology and surface impacts of

1292 atmospheric rivers on West Antarctica. *The Cryosphere*, 17, 865-881. <https://doi.org/10.5194/tc-17-865-2023>

1293

1294

1295 McLennan, M. L., Lenaerts, J. T. M., Shields, C., Wille, J. D. (2022) Contribution of atmospheric rivers to  
1296 Antarctic precipitation. *Geophysical Research Letters*, 49, e2022GL100585.  
1297 <https://doi.org/10.1029/2022GL100585>

1298

1299 Meredith, M. P., Stammerjohn, S. E., Ducklow, H. W., Leng, M. J., Arrowsmith, C., Brearley, J. A.,  
1300 Venables, H. J., Barham, M., van Wessem, J. M., Schofield, O., Waite, N. (2021) Local- and large-scale  
1301 drivers of variability in the coastal freshwater budget of the Western Antarctic Peninsula. *Journal of  
1302 Geophysical Research: Oceans*, 126, e2021JC017172. <https://doi.org/10.1029/2021JC017172>

1303

1304 Miles, B. W. J., Stokes, C. R., Jamieson, S. S. R. (2017) Simultaneous disintegration of outlet glaciers in  
1305 Porpoise Bay (Wilkes Land), East Antarctica, driven by sea ice break-up. *The Cryosphere*, 11, 427-442.  
1306 <https://doi.org/10.5194/tc-11-427-2017>

1307

1308 Mills, C. M. (2011) Modification of the Weather Research and Forecasting Model's treatment of sea ice  
1309 albedo over the Arctic Ocean. WRF3.3.1 Code Submission Doc., 2 pp. Accessed on 19 August 2024,  
1310 available online at  
1311 [http://publish.illinois.edu/catrinmills/files/2012/10/Mills\\_WRFIceAlbedoProj\\_Summary.pdf](http://publish.illinois.edu/catrinmills/files/2012/10/Mills_WRFIceAlbedoProj_Summary.pdf)

1312

1313 Montini, T. L., Jones, C., Carvalho, L. M. V. (2019) The South American low-level jet: A new climatology,  
1314 variability, and changes. *Journal of Geophysical Research: Atmospheres*, 124, 1200-1218.  
1315 <https://doi.org/10.1029/2018JD029634>

1316

1317 Morrison, H., Milbrandt, J. A. (2015) Parameterization of Cloud Microphysics Based on the Prediction of  
1318 Bulk Ice Particle Properties. Part I: Scheme Description and Idealized Tests. *Journal of the Atmospheric  
1319 Sciences*, 72, 287-311. <https://doi.org/10.1175/JAS-D-14-0065.1>

1320

1321 Nakanishi, M., Niino, H. (2006) An improved Mellor-Yamada level-3 model: Its numerical stability and  
1322 application to a regional prediction of advection fog. *Boundary-Layer Meteorology*, 119, 397-407.  
1323 <https://doi.org/10.1007/s10546-005-9030-8>

1324

1325 Nelli, N. R., Francis, D., Fonseca, R., Abida, R., Weston, M., Wehbe, Y., Al Hosary, T. (2021) The  
1326 atmospheric controls of extreme convective events over the southern Arabian Peninsula during the spring  
1327 season. *Atmospheric Research*, 262, 105788. <https://doi.org/10.1016/j.atmosres.2021.105788>

1328

1329 Niu, G.-Y., Yang, Z.-L., Mitchell, K. E., Chen, F., Ek, M. B., Barlage, M., Kumar, A., Manning, K., Niyogi,  
1330 D., Rosero, E., Tewari, M., Xia, Y. (2011) The community Noah land surface model with  
1331 multiparameterization options (Noah-MP): 1. Model description and evaluation with local-scale  
1332 measurements. *Journal of Geophysical Research*, 116, D12109. <https://doi.org/10.1029/2010JD015139>

1333

1334 NOAA ARL (2024) HYSPLIT for Linux - Public (unregistered) version download [Software]. National  
1335 Oceanic and Atmospheric Administration Air Resources Laboratory. Accessed on 04 July, available online  
1336 at [https://www.ready.noaa.gov/HYSPLIT\\_linuxtri](https://www.ready.noaa.gov/HYSPLIT_linuxtri)

1337

1338 NOAA/NWS (2024) Cold & Warm Episodes by Season [Dataset]. National Oceanic and Atmospheric  
1339 Administration / National Weather Service Climate Prediction Center. Accessed on 24 July, available  
1340 online at [https://origin.cpc.ncep.noaa.gov/products/analysis\\_monitoring/ensostuff/ONI\\_v5.php](https://origin.cpc.ncep.noaa.gov/products/analysis_monitoring/ensostuff/ONI_v5.php)

1341

1342 Oliveira, F. N. M., Carvalho, L. M. V., Ambrizzi, T. (2013) A new climatology for Southern Hemisphere  
1343 blockings in the winter and the combine defect of ENSO and SAM phases. International Journal of  
1344 Climatology, 34, 676-1692. <https://doi.org/10.1002/joc.3795>

1345

1346 Oolman, L. (2025) University of Wyoming - atmospheric soundings [Dataset]. Accessed on 04 July 2024,  
1347 data available online at <https://weather.uwyo.edu/upperair/sounding.html>

1348

1349 Parkinson, C. L. (2019) A 40-y record reveals gradual Antarctic sea ice increases followed by decreases at  
1350 rates far exceeding the rates seen in the Arctic. Environmental Sciences, 116, 14414-14423.  
1351 <https://doi.org/10.1073/pnas.1906556116>

1352

1353 Parkinson, C. L., Cavalieri, D. J. (2012) Antarctic sea ice variability and trends, 1979-2010. The  
1354 Cryosphere, 6, 871-880. <https://doi.org/10.5194/tc-6-871-2012>

1355

1356 Plante, M., Lemieux, J.-F., Tremblay, L. B., Tivy, A., Angnatok, J., Roy, F., Smith, G., Dupont, F., Turner,  
1357 A. K. (2024) Using Icemap to reproduce ice mass balance buoy observations in landfast ice: improvements  
1358 from the mushy-layer thermodynamics. The Cryosphere, 18, 1685-1708. <https://doi.org/10.5194/tc-18-1685-2024>

1360

1361 Pook, M. J., Risbey, J. S., McIntosh, P. C., Ummenhofer, C. C., Marshall, A. G., Meyers, G. A. (2013) The  
1362 seasonal cycle of blocking and associated physical mechanisms in the Australian region and relationship  
1363 with rainfall. Monthly Weather Review, 141, 4534-4553. <https://doi.org/10.1175/MWR-D-13-00040.1>

1364

1365 Purich, A., Doddridge, E. W. (2023) Record low Antarctic sea ice coverage indicates a new sea ice state.  
1366 Communications Earth & Environment, 4, 314. <https://doi.org/10.1038/s43247-023-00961-9>

1367

1368 PWRF (2024) The Polar WRF. Byrd Polar and Climate Research Center. The Ohio State University  
1369 [Model]. Accessed on 08 April 2024, available online at <https://polarmet.osu.edu/PWRF/>.

1370

1371 Quan, J., Di, Z., Duan, Q., Gong, W., Wang, C., Gan, Y., Ye, A., Miao, C. (2016) An evaluation of  
1372 parametric sensitivities of different meteorological variables simulated by the WRF model. Quarterly  
1373 Journal of the Royal Meteorological Society, 142, 2925-2934. <https://doi.org/10.1002/qj.2885>

1374

1375 Raphael, M. N., Hobbs, W., Wainer, I. (2011) The effect of Antarctic sea ice on the Southern Hemisphere  
1376 atmosphere during the southern summer. Climate Dynamics, 36, 1403-1417.  
1377 <https://doi.org/10.1007/s00382-010-0892-1>

1378  
1379 Rauber, R., M., Hu, H., Dominguez, F., Nesbitt, S. W., McFarquhar, G. M., Zaremba, T. J., Finlon, J. A.  
1380 (2020) Structure of an atmospheric river over Australia and the Southern Ocean. Part I: Tropical and  
1381 midlatitude water vapor fluxes. *Journal of Geophysical Research: Atmospheres*, 125, e2020JD032513.  
1382 <https://doi.org/10.1029/2020JD032513>  
1383  
1384 Reid, P., Stammerjohn, S., Massom, R. A., Barreira, S., Scambos, T., Lieser, J. L. (2024) Sea-ice extent,  
1385 concentration, and seasonality [in “State of the Climate in 2023”]. *Bulletin of the American Meteorological  
1386 Society*, 105, 350-353. <https://doi.org/10.1175/BAMS-D-24-0099.1>  
1387  
1388 Riihelä, A., Bright, R. M., Anttila, K. (2021) Recent strengthening of snow and ice albedo feedback driven  
1389 by Antarctic sea-ice loss. *Nature Geosciences*, 14, 832-836. <https://doi.org/10.1038/s41561-021-00841-x>  
1390  
1391 Roach, L. A., Dorr, J., Holmes, C. R., Massonnet, F., BLockley, E. W., Notz, D., Rackow, T., Raphael, M.  
1392 N., O’Farrell, S. P., Bailey, D. A., Bitz, C. M. (2020) Antarctic Sea Ice Area in CMIP6. *Geophysical  
1393 Research Letters*, 47, e2019GL086729. <https://doi.org/10.1029/2019GL086729>  
1394  
1395 Schroeter, S., Sandery, P. A. (2022) Large-ensemble analysis of Antarctic sea ice model sensitivity to  
1396 parameter uncertainty. *Ocean Modeling*, 177, 102090. <https://doi.org/10.1016/j.ocemod.2022.102090>  
1397  
1398 Sledd, A., Shupe, M. D., Solomon, A., Cox, C. J., Perovich, D., Lei, R. (2024) Snow thermal conductivity  
1399 and conductive flux in the Central Arctic: Estimates from observations and implications for models.  
1400 *Elements: Science of the Anthropocene*, 12, 00086. <https://doi.org/10.1525/elementa.2023.00086>  
1401  
1402 Skamarock, W. C., Klemp, J. B., Dudhia, J., Gill, D. O., Liu, Z., Berner, J., Wang, W., Powers, J. G., Duda,  
1403 M. G., Barker, D., Huang, X.-Y. (2019) Description of the Advanced Research WRF Model Version 4.3  
1404 (No. NCAR/TN-556+STR). Accessed on 03 June 2024, available online at  
1405 <https://opensky.ucar.edu/islandora/object/opensky:2898>  
1406  
1407 Spreen, G., Kaleschke, L., Heygster, G. (2008) Sea ice remote sensing using AMSR-E 89-GHz channels.  
1408 *Journal of Geophysical Research*, 113, C02S03. <https://doi.org/10.1029/2005JC003384>  
1409  
1410 Stein, A. F., Draxler, R. R., Rolph, G. D., Stunder, B. J. B., Cohen, M. D., Ngan, F. (2015) NOAA’s  
1411 HYSPLIT atmospheric transport and dispersion modeling system. *Bulletin of the American Meteorological  
1412 Society*, 96, 2059-2077. <https://doi.org/10.1175/BAMS-D-14-00110.1>  
1413  
1414 Szapiro, N., Cavallo, S. (2018) TPVTrack v1.0: A watershed segmentation and overlap correspondence  
1415 method for tracking tropopause polar vortices. *Geoscientific Model Development*, 11, 5173-5187.  
1416 <https://doi.org/10.5194/gmd-11-5173-2018>  
1417  
1418 Takaya, K., Nakamura, H. (2001) A Formulation of a Phase-Independent Wave-Activity Flux for Stationary  
and Migratory Quasigeostrophic Eddies on a Zonally Varying Basic Flow. *Journal of the Atmospheric  
Sciences*, 58, 608-627. [https://doi.org/10.1175/1520-0469\(2001\)058<0608:AFOAPI>2.0.CO;2](https://doi.org/10.1175/1520-0469(2001)058<0608:AFOAPI>2.0.CO;2)

1419 Tewari, M., Chen, F., Wang, W., Dudhia, J., Lemone, M. A., Mitchell, K. E., et al. (2004) Implementation  
1420 and verification of the unified NOAH land surface model in the WRF model. *20th Conference on Weather  
1421 Analysis and Forecasting/16th Conference on Numerical Weather Prediction*, Seattle, W, American  
1422 Meteorological Society, 14.2.a. Accessed on 25 January 2024, available online at  
1423 <https://opensky.ucar.edu/islandora/object/conference:1576>

1424 Tewari, K., Mishra, S. K., Salunke, P., Ozawa, H., Dewan, A. (2023) Potential effects of the projected  
1425 Antarctic sea-ice loss on the climate system. *Climate Dynamics*, 60, 589-601.  
1426 <https://doi.org/10.1007/s00382-022-06320-2>

1427 Thomas, D (editor) (2017) Sea Ice. 3rd Edition. Wiley-Blackwell, New York (USA) and Oxford (UK), 664  
1428 pp. ISBN: 978-1-118-77838-8.

1429 Terpstra, A., Gorodetskaya, I. V., Sodemann, H. (2021) Linking sub-tropical evaporation and extreme  
1430 precipitation over East Antarctica: An atmospheric river case study. *Journal of Geophysical Research: Atmospheres*, 126, e2020JD033617. <https://doi.org/10.1029/2020JD033617>

1432 Trusel, L. D., Kromer, J. D., Datta, R. T. (2023) Atmospheric Response to Antarctic Sea-Ice Reductions  
1433 Drives Ice Sheet Surface Mass Balance Increase. *Journal of Climate*, 19, 6879-6896.  
1434 <https://doi.org/10.1175/JCLI-D-23-0056.1>

1435 University of Bremen (UoB) (2024) Sea Ice Remote Sensing, Data Archived. Accessed on 01 August 2024,  
1436 available online at <https://data.seaice.uni-bremen.de/>.

1437 Vignon, E., Alexander, S. P., DeMott, P. J., Sotiropoulou, G., Gerber, F., Hill, T. C. J., Marchand, R.,  
1438 Nenes, A., Berne, A. (2021) Challenging and improving the simulation of mid-level mixed-phase clouds  
1439 over the high-latitude Southern Ocean. *Journal of Geophysical Research: Atmospheres*, 126,  
1440 e2020JD033490. <https://doi.org/10.1029/2022JD033490>

1441 Vignon, E., Traulle, O., Berne, A. (2019) On the fine vertical structure of the low troposphere over coastal  
1442 margins of East Antarctica. *Atmospheric Chemistry and Physics*, 19, 4659-4683.  
1443 <https://doi.org/10.5194/acp-19-4659-2019>

1445 Wallace, J. M., Hobbs, P. V. (2006) Atmospheric science: An introductory survey. 504 pp. Academic Press  
1446 Inc., second edition. ISBN-10: 012732951X, ISBN-13: 978-0127329512.

1449 Wang, Z., Li, Z., Zeng, J., Liang, S., Zhang, P., Tang, F., Chen, S., Ma, X. (2020) Spatial and temporal  
1450 variations of Arctic sea ice from 2002 to 2017. *Earth and Space Science*, 7, e2020EA001278.  
1451 <https://doi.org/10.1029/2020EA001278>

1453 Wang, M., Linhardt, F., Lion, V., Oppelt, N. (2024) Melt Pond Evolution along the MOSAiC Drift:  
1454 Insights from Remote Sensing and Modeling. *Remote Sensing*, 16, 3748.  
1455 <https://doi.org/10.3390/rs16193748>

1456

1457 Wang, J., Massonnet, F., Goosse, H., Luo, H., Barthelemy, A., Wang, Q. (2024) Synergistic atmosphere-  
1458 ocean-ice influences have driven the 2023 all-time Antarctic sea-ice record low. *Communications Earth &*  
1459 *Environment*, 5, 415. <https://doi.org/10.1038/s43247-024-01523-3>

1460

1461 Webster, M., Gerland, S., Holland, M., Hunke, E., Kwok, R., Lecomte, O., Masson, R., Perovich, D., Sturm,  
1462 M. (2018) Snow in the changing sea-ice system. *Nature Climate Change*, 8, 945-954.  
1463 <https://doi.org/10.1038/s41558-018-0286-7>

1464

1465 Wille, J. D., Alexander, S. P., Amory, C., Baiman, R., Barthelemy, L., Bergstrom, D. M., Berne, A., Binder,  
1466 H., Blanchet, J., Bozkurt, D., Bracegirdle, T. J., Casado, M., Choi, T., Clem, K. R., Cordron, F., Datta, R.,  
1467 Di Battista, S., Favier, V., Francis, D., Fraser, A. D., Fourre, E., Garreaud, R. D., Genthon, C.,  
1468 Goorodetskaya, I. V., Gonzalez-Herrero, S., Heinrich, V. J., Hubert, G., Joos, H., Kim, S.-J., King, J. C.,  
1469 Kittel, C., Landais, A., Lazzara, M., Leonard, G. H., Lieser, J. L., Maclennan, M., Mikolajczyk, D., Neff,  
1470 P., Ollivier, I., Picard, G., Pohl, B., Ralph, F. M., Rowe, P., Schlosser, E., Shields, C. A., Smith, I. J.,  
1471 Sprenger, M., Trusel, L., Udy, D., Vance, T., Vignon, E., Walker, C., Wever, N., Zou, X. (2024a) The  
1472 Extraordinary March 2022 East Antarctica “Heat” Wave. Part I: Observations and Meteorological Drivers.  
1473 *Journal of Climate*, 37, 757-778. <https://doi.org/10.1175/JCLI-D-23-0175.1>

1474

1475 Wille, J. D., Alexander, S. P., Amory, C., Baiman, R., Barthelemy, L., Bergstrom, D. M., Berne, A., Binder,  
1476 H., Blanchet, J., Bozkurt, D., Bracegirdle, T. J., Casado, M., Choi, T., Clem, K. R., Cordron, F., Datta, R.,  
1477 Di Battista, S., Favier, V., Francis, D., Fraser, A. D., Fourre, E., Garreaud, R. D., Genthon, C.,  
1478 Goorodetskaya, I. V., Gonzalez-Herrero, S., Heinrich, V. J., Hubert, G., Joos, H., Kim, S.-J., King, J. C.,  
1479 Kittel, C., Landais, A., Lazzara, M., Leonard, G. H., Lieser, J. L., Maclennan, M., Mikolajczyk, D., Neff,  
1480 P., Ollivier, I., Picard, G., Pohl, B., Ralph, F. M., Rowe, P., Schlosser, E., Shields, C. A., Smith, I. J.,  
1481 Sprenger, M., Trusel, L., Udy, D., Vance, T., Vignon, E., Walker, C., Wever, N., Zou, X. (2024b) The  
1482 Extraordinary March 2022 East Antarctica “Heat” Wave. Part II: Impacts on the Antarctic Ice Sheet. *Journal*  
1483 *of Climate*, 37, 779-799. <https://doi.org/10.1175/JCLI-D-23-0176.1>

1484

1485 Wille, J. D., Bromwich, D. H., Cassano, J. J., Nigro, M. A., Mateling, M. E., Lazzara, M. A. (2017)  
1486 Evaluation of the AMPS Boundary Layer Simulations on the Ross Ice Shelf, Antarctica, with Unmanned  
1487 Aircraft Observations. *Journal of Applied Meteorology and Climatology*, 56, 2239-2258.  
1488 <https://doi.org/10.1175/JAMC-D-16-0339.1>

1489

1490 Wille, J. D., Bromwich, D. H., Nigro, M. A., Cassano, J. J., Mateling, M., Lazzara, M. A., Wang, S.-H.  
1491 (2016) Evaluation of the AMPS Boundary Layer Simulations on the Ross Ice Shelf with Tower  
1492 Observations. *Journal of Applied Meteorology and Climatology*, 55, 2349-2367.  
1493 <https://doi.org/10.1175/JAMC-D-16-0032.1>

1494

1495 Wille, J. D., Favier, V., Dufour, A., Gorodetskaya, I. V., Turner, J., Agosta, C., Codron, F. (2019) West  
1496 Antarctic surface melt triggered by atmospheric rivers. *Nature Geoscience*, 12, 911-916.  
1497 <https://doi.org/10.1038/s41561-019-0460-1>

1498

1499 Wille, J. D., Favier, V., Gorodetskaya, I. V., Agosta, C., Baiman, R., Barrett, J. E., Barthelemy, L., Boza,  
1500 B., Bozkurt, D., Casado, M., Chyhareva, A., Clem, K. R., Codron, F., Datta, R. T., Duran-Alarcon, C.,

1501 Francis, D., Hoffman, A. O., Kolbe, M., Krakosvska, S., Linscott, G., Maclennan, M. L., Mattingly, K. S.,  
1502 Mu, Y., Pohl, B., Santos, C. L.-D., Shields, C. A., Toker, E., Winters, A. C., Yin, Z., Zou, X., Zhang, C.,  
1503 Zhang, Z. (2025) Atmospheric rivers in Antarctica. *Nature Reviews Earth & Environment*, 6, 178-192.  
1504 <https://doi.org/10.1038/s43017-024-00638-7>

1505 Wille, J. D., Favier, V., Gorodetskaya, I. V., Agosta, C., Kittel, C., Beeman, J. C., Jourdain, N. C., Lenaerts,  
1506 J. T. M., Codron, F. (2021) Antarctic atmospheric river climatology and precipitation impacts. *Journal of*  
1507 *Geophysical Research: Atmospheres*, 126, e2020JD033788. <https://doi.org/10.1029/2020JD0033788>

1508 Wille, J. D., Pohl, B., Favier, V., Winters, A. C., Baiman, R., Cavallo, S. M., Leroy-Dos Santos, C., Clem,  
1509 K., Udy, D. G., Vance, T. R., Gorodetskaya, I., Codron, F., Berchet, A. (2024c) Examining atmospheric  
1510 river life cycles in East Antarctica. *Journal of Geophysical Research: Atmospheres*, 129, e2023JD039970.  
1511 <https://doi.org/10.1029/2023JD039970>

1512 Williams, N., Byrne, N., Feltham, D., Van Leeuwen, P. J., Bannister, R., Schroeder, D., Ridout, A., Nerger,  
1513 L. (2023) The effects of assimilating a sub-grid-scale sea ice thickness distribution in a new Arctic sea ice  
1514 data assimilation system. *The Cryosphere*, 17, 2509-2532. <https://doi.org/10.5194/tc-17-2509-2023>

1515 Worby, A. P., Steer, A., Lieser, J. L., Heil, P., Yi, D., Markus, T., Allison, I., Massom, R. A., Galin, N.,  
1516 Zwally, J. (2011) Regional-scale sea-ice and snow thickness distribution from in situ and satellite  
1517 measurements over East Antarctica during SIPEX 2007. *Deep Sea Research Part II: Topical Studies in*  
1518 *Oceanography*, 58, 1125-1136. <https://doi.org/10.1016/j.dsr2.2010.12.001>

1519 Xie, H., Ackley, S. F., Yi, D., Zwally, H. J., Wagner, P., Weissling, B., Lewis, M., Ye, K. (2011) Sea-ice  
1520 thickness distribution of the Bellingshausen Sea from surface measurements and ICESat altimetry. *Deep*  
1521 *Sea Research Part II: Topical Studies in Oceanography*, 58, 1039-1051.  
1522 <https://doi.org/10.1016/j.dsr2.2010.10.038>

1523 Xue, J., Xiao, Z., Bromwich, D. H., Bai, L. (2022) Polar WRF V4.1.1 simulation and evaluation for the  
1524 Antarctic and Southern Ocean. *Frontiers of Earth Science*, 16, 1005-1024. <https://doi.org/10.1007/s11707-022-0971-8>

1525 Yang, J., Xiao, X., Liu, J., Li, Qin, D. (2021) Variability of Antarctic sea ice extent over the past 200 years.  
1526 *Science Bulletin*, 66, 2394-2404. <https://doi.org/10.1016/j.scib.2021.07.028>

1527 Zhang, J. (2014) Modeling the Impact of Wind Intensification on Antarctic Sea Ice Volume. *Journal of*  
1528 *Climate*, 27, 202-214. <https://doi.org/10.1175/JCLI-D-12-00139.1>

1529 Zhang, R., Screen, J. A. (2021) Diverse Eurasian winter temperature responses to Barents-Kara sea ice  
1530 anomalies of different magnitudes and seasonality. *Geophysical Research Letters*, 48, e2021GL092726.  
1531 <https://doi.org/10.1029/2021GL092726>

1532 Zeng, X., Beljaars, A. (2005) A prognostic scheme of sea surface skin temperature for modeling and data  
1533 assimilation. *Geophysical Research Letters*, 32, L14605. <https://doi.org/10.1029/2005GL023030>

1545

1546 Zou, X., Bromwich, D. H., Montenegro, A., Wang, S.-H., Bai, L. (2021a) Major surface melting over the  
1547 Ross Ice Shelf part I: Foehn effect. *Quarterly Journal of the Royal Meteorological Society*, 147, 2874-2894.  
1548 <https://doi.org/10.1002/qj.4104>

1549

1550 Zou, X., Bromwich, D. H., Montenegro, A., Wang, S.-H., Bai, L. (2021b) Major surface melting over the  
1551 Ross Ice Shelf part II: Surface energy balance. *Quarterly Journal of the Royal Meteorological Society*, 147,  
1552 2895-2916. <https://doi.org/10.1002/qj.4105>

1553

1554 Zou, X., Rowe, P. M., Gorodetskaya, I., Bromwich, D. H., Lazzara, M. A., Cordero, R. R., Zhang, Z.,  
1555 Kawzenuk, B., Cordeira, J. M., Wille, J. D., Ralph, F. M., Bai, L.-S. (2023) Strong warming over the  
1556 Antarctic Peninsula during combined atmospheric River and foehn events: Contribution of shortwave  
1557 radiation and turbulence. *Journal of Geophysical Research: Atmospheres*, 128, e2022JD038138.  
1558 <https://doi.org/10.1029/2022JD038138>